The Dissertation Committee for Bin Yang Certifies that this is the approved version of the following dissertation:

Optical and Structural Property Mapping of Soft Tissues Using Spatial Frequency Domain Imaging

Committee:

James W. Tunnell, Supervisor

Sunil Krishnan

Jason S. Reichenberg

Hsin-Chih Yeh

Michael Sacks

Optical and Structural Property Mapping of Soft Tissues Using Spatial Frequency Domain Imaging

by

Bin Yang, B.S.; B.S.; M.S.

Dissertation

Presented to the Faculty of the Graduate School of

The University of Texas at Austin

in Partial Fulfillment

of the Requirements

for the Degree of

Doctor of Philosophy

The University of Texas at Austin

August 2015

Dedication

To my parents, wife and son

Acknowledgements

First and foremost, I would like to thank Dr. James Tunnell for his invaluable guidance and support. I appreciate and enjoy the freedom and encouragement that stimulated me to explore different research directions. I always feel grateful to have you as my advisor!

I would like to thank our collaborators who played a part in my degree. Dr. Jason Reichenberg at Seton Healthcare is genuinely interested in new technologies in dermatology. Thank you for providing me the opportunity to conduct clinical skin studies. Thank you to Poppy Poth our clinic study coordinator for arranging each clinic visit and for making sure that the clinical study went smoothly. I would like to thank Dr. Michael Sacks for providing me knowledge and guidance in biomechanics study. Especially I would like to thank John Lesicko for contributing to pSFDI project: it was a great pleasure to work with you. Also I would like to thank Dr. Sunil Krishnan from UT MD. Anderson for providing me small animals and facilities for fluorescence imaging study. Thank you Dr. Tim Yeh for invaluable advice on presentation skills and for willingness to be part of my dissertation committee.

Thank you also to my colleagues, Sam Lim, Varun Pattani, Manu Sharma, Sheldon Bish, Austin Moy, Ricky Hennessy, Will Goth and Xu Feng, for their help in the laboratory and discussions on problems that occurred.

To my parents and my wife, Hanyu, thank you for your undying encouragement, love and support throughout the years. To my little Bowen, you are truly an adorable and sometimes troublesome kid! I love you all!

Optical and Structural Property Mapping of Soft Tissues Using Spatial Frequency Domain Imaging

Bin Yang, Ph.D.

The University of Texas at Austin, 2015

Supervisor: James W. Tunnell

Tissue optical properties, absorption, scattering and fluorescence, reveal important information about health, and holds the potential for non-invasive diagnosis and therefore earlier treatment for many diseases. On the other hand, tissue structure determines its function. Studying tissue structural properties helps us better understand structure-function relationship. Optical imaging is an ideal tool to study these tissue properties. However, conventional optical imaging techniques have limitations, such as not being able to quantitatively evaluate tissue absorption and scattering properties and only providing volumetrically averaged quantities with no depth control capability. To better study tissue properties, we integrated spatial frequency domain imaging (SFDI) with conventional reflectance imaging modalities. SFDI is a non-invasive, non-contact wide-field imaging technique which utilizes structured illumination to probe tissues. SFDI imaging is able to accurately quantify tissue optical properties. By adjusting spatial frequency, the imaging depth can be tuned which allows for depth controlled imaging. Especially at high spatial frequency, SFDI reflectance image is more sensitive to tissue scattering property than absorption property. The imaging capability of SFDI allows for studying tissue properties from a whole new perspective. In our study, we developed both benchtop and handheld SFDI imaging systems to accommodate different applications. By evaluating tissue optical

properties, we corrected attenuation in fluorescence imaging using an analytical model; and we quantified optical and physical properties of skin diseases. By imaging at high spatial frequency, we demonstrated that absorption in fluorescence imaging can also be reduced because of a reduced imaging depth. This correction can be performed in real-time at 19 frames/second. Furthermore, fibrous structures orientation from the superficial layer can be accurately quantified in a multi-layered sample by limiting imaging depth. Finally, we color rendered SFDI reflectance image at high spatial frequency to reveal structural changes in skin lesions.

Table of Contents

List of Figures

CHAPTER 1 : INTRODUCTION

1.1 MOTIVATION

Conventional wide-field optical imaging methods have been widely used in visualization and characterization of different types of tissues (1-5). Optical imaging techniques are attractive because they typically utilize non-ionizing radiation, namely light, to interrogate tissue in a non-invasive way. Rich optical and physiological information then can be extracted. Fluorescence imaging is an ideal tool to visualize local endogenous biochemical composition information. In conjunction with targeted exogenous fluorescent contrast agent, fluorescence imaging can be used to identify and help resect solid tumors (6, 7). Reflectance imaging at multiple wavelengths reveals tissue absorption and scattering properties, and provides insights into biochromophore composition and distribution (8, 9). Polarized light imaging has the ability to probe tissue structural information, which is important to study structure-function relationship (10-12). However, these imaging modalities also have limitations. Although absorption and scattering provide the contrast in reflectance imaging, they generate problems in fluorescence imaging. The fluorescence intensity is attenuated due to tissue attenuation and scattering, which makes quantitative fluorescence imaging challenging(13). Conventional hyperspectral reflectance imaging is sensitive to reflectance or albedo, which is a mixed contribution from both absorption and scattering(2, 14). However, it does not have the ability to separate absorption from scattering which limits its usefulness. Furthermore, conventional wide-field imaging techniques does not have any capability to control imaging depth and can only provide

depth averaged information (15). Biological tissues are typical multi-layered, therefore without proper depth control, superficial layer specific information can't be accurately quantified. These limitation can be mitigated by integrating conventional wide-field imaging technique with newly developed spatial frequency domain imaging (SFDI) (16). SFDI imaging is able to quantify tissue optical properties in wide field non-invasively using structured illumination. Furthermore, by varying spatial frequency of illumination pattern, the imaging depth can be controlled. By integrating SFDI imaging, both imaging capability and accuracy are improved for conventional wide-field imaging.

The objective of my dissertation was to develop and integrate SFDI imaging system with multiple imaging techniques: fluorescence imaging, polarized light imaging and hyperspectral imaging; and to demonstrate enhanced imaging capability with the integrated imaging technologies in multiple applications

1.2 BACKGROUND AND SIGNIFICANCE

1.2.1 Optical Properties of Biological Tissues

In biomedical optics, optical properties of tissue are of particular importance in investigating many types of diseases and hold the potential for non-invasive diagnosis especially for cancers. Optical properties commonly used for diagnostics include tissue absorption and scattering properties. In biological tissue, absorption is mainly from hemoglobin and melanin, and in higher wavelength range (>1000nm), water also becomes a main absorber (17). The concentration of biochromophore can be used as an indicator for many diseases. For example, there are more blood vessels found inside a solid tumor to

satisfy the higher metabolic need of cancer cells. For this reason, solid tumors often have higher blood content(18). The scattering property is associated with local biological microstructures, ranging from collagen fibrils, to mitochondria and nuclei, and to cells. The size change of microstructures is linked with many diseases, especially cancers. Using optical techniques, it was reported that in precancerous epithelial cells, nuclei are enlarged, which can be used as to detect cancers at an early stage (19). Optical properties reveal valuable information regarding tissue composition and structural integrity, and can be used for non-invasive diagnosis of many diseases.

1.2.3 Spatial Frequency Domain Imaging

The challenge of quantifying the optical properties of the biological tissue is to separate the absorption from scattering. Conventional wide field reflectance imaging technique can only image reflectance or 'albedo', which is a mixed contribution from both absorption and scattering effects. Although it is possible to quantify the tissue optical properties, almost all of these techniques can only perform localized point measurement.

SFDI imaging was recently developed to quantify the optical properties of the turbid medium in wide field (16). SFDI imaging provides high spatial resolution which is typically <1mm. The SFDI uses structured illumination to interact with the turbid tissue. The illumination field is typically a two-dimensional sinusoidal pattern. As the illumination pattern propagates into the tissue, the pattern becomes attenuated due to the absorption and scattering events. Such modification is dependent on the turbidity of the sample. The diffuse reflectance at the surface carries the information of the optical properties of the

sample. Multiple techniques has been developed to extract optical properties from the measured reflectance images. The standard diffusion approximation was developed to model the modulated reflectance and to extract optical properties (20). This method only works for scattering dominant medium. Thus, the application was limited. For the biological tissue, it is typically in the near-infrared (NIR) wavelength range. However, in the visible range, tissue absorption is at the same order of magnitude as the scattering, thus the diffusion approximation is no longer valid. As a result, both Monte-Carlo and experiment based look-up table (LUT) methods were later developed (21), which extended the usefulness of SFDI from NIR to visible wavelength range. The reflectance from a set of phantoms with known optical properties are either simulated or experimentally measured. Based on the reflectance, a LUT can be generated using a forward model. By using the LUT inversely, the optical properties with unknown optical properties can be accurately retrieved. Although it has only been 10 years since SFDI imaging was first introduced in 2005, SFDI imaging has been used in many biomedical applications including studies in skin flap vascular occlusions (22), burn injury(23), skin surveillance and optical biopsy (24) .

1.2.4 Structured Illumination at High Spatial Frequency

In conventional reflectance imaging, the imaging depth is determined by both absorption and scattering properties of the sample at the illumination wavelength and the effective imaging depth is $\delta_{eff}^{'} = (\sqrt{3\mu_a(\mu_a + \mu_s^{'})})^{-1}$, where μ_a and $\mu_s^{'}$ are the absorption coefficient and reduced scattering coefficient, respectively. For biological tissues, the imaging depth can

be up to several millimeters under NIR illumination. The imaging depth can't be adjusted and the reflectance image is integrated over the imaging depth. Imaging deeper also means larger diffuse background, which reduces resolution. With the structured illumination, the imaging depth is determined by tissue optical properties AND spatial frequency. In scattering dominant medium, the effective penetration depth is describe as $\delta_{eff}^{'} = (\sqrt{3\mu_a(\mu_a + \mu_s^{'}) + (2\pi f)^2})^{-1}$, where f is the spatial frequency(20). The optical properties determine maximal depth that can be imaged. By tuning the spatial frequency, a shallower imaging depth can be achieved. At a high spatial frequency, unique reflectance properties can be observed. At a high spatial frequency, the modulated reflectance is only responsible for an imaging depth as shallow as a few hundreds of micrometers. At this depth, the tissue absorption does not attenuate the modulated reflectance significantly. On the other hand, because of shallow imaging depth, the photons in modulated reflectance undergo less scattering events and they are less diffuse. Thus, the scattering properties of the sample surface can be enhanced.

This property has a significant impact on biological tissue imaging. Many types of biological tissues are naturally multi-layered, such as skin. Conventional reflectance imaging only provides through-thickness contrast, which may integrate over multiple layers. Imaging at high spatial frequency makes it possible to only look at superficial layer, which often times are epithelial layer. Many types of cancer develop in the epithelial layer before they invades into deeper tissue. Imaging epithelial layer provides a way to characterize its optical properties especially the scattering properties.

1.2.5 SFDI Based Optical Imaging

SFDI imaging alone is able to accurately quantify the optical properties and to control the imaging depth. When SFDI imaging is incorporated into other imaging modalities, even greater imaging capability can be achieved. The following three imaging technologies have been studied. Detailed description and application will be discussed in following chapters.

1.2.5.1 Hyperspectral SFDI imaging

Hyperspectral reflectance imaging is normally used to examining the spectral features over the wavelength of interest. The spectral features could be associated with either local absorption property change, for example angiogenesis and pigmentation, or scattering property change, for example enlarged nuclei. While the hyperspectral imaging reveals such spectral information, it is an overall contribution from both absorption and scattering and its individual contribution is hard to quantify.

The SFDI imaging greatly expands the usefulness of the hyperspectral imaging by quantifying both absorption and reduced scattering coefficients at each individual wavelength. With the absorption coefficients, the biochromophore concentration and oxygen saturation can be further extracted, which is essentially performing ‘optical biopsy’. Hyperspectral SFDI imaging enables a new way to quantitatively evaluate the tissue properties.

1.2.5.2 Fluorescence imaging and attenuation correction

Fluorescence imaging is widely used in biomedical applications. Typical endogenous fluorophore found in biological samples are either associated with structural matrix of tissues such as collagen and elastin or cellular metabolic pathways such as NAD(P)H (2). By quantifying the endogenous fluorescence, important structural or metabolic rate changes can be studied, which potentially have the diagnostic power in many diseases. Georgakoudi *et al* showed that lower collagen fluorescence and higher NAD(P)H fluorescence was found in dysplastic tissues compared to normal tissues (25). The decreased collagen fluorescence could be qualitatively understood as collagen crosslink in extracellular matrix are cleaved by increased collagenases in cancerous tissues, which reduces the collagen concentration (15). Higher NAD(P)H fluorescence may be related to the increased metabolism rate in cancer cells.

On the other hand, exogenous fluorescent probes are typically used as contrast agents to in fluorescence imaging. Recently, molecular fluorescent probes have been engineered to study many types of cancers. The characteristics of cancer cells, such as epithelia growth factor (EGF) receptor, increased metabolism, integrin $\alpha v\beta 3$ receptor, permit specifically engineered fluorescence probes to target and accumulate on cancer cells (26), which enables a way to visualize and localize the tumor. More importantly, visualization of the tumor can provide a visual feedback during tumor resection surgery, which may lead to more complete resection. Van Dam *et al* demonstrated the first human results on intraoperative ovarian cancer imaging and resection (27). Using the fluorescence imaging to map the sentinel lymph node was also reported (13)

The fluorescence intensity is determined by many factors such as local fluorophore concentration, chemical environment and tissue attenuation. Tissue attenuation especially the absorption distorts the fluorescence intensity. Thus, the imaged fluorescence does not faithfully reflect the fluorophore concentration and distribution, and may complicate the decision making. Different techniques have been developed to compensate the attenuation effects by employing model based correction, empirical correction and experimental correction. Coremans *et al* demonstrated that taking the ratio of fluorescence and the reflectance at excitation wavelength, semi-quantitative measure for NADH fluorescence of blood perfused rat heart can be achieved (18). This ratio technique was recently used in sentinel lymph node (13) and imaging guided tumor resection (27, 28). A photon migration model based correction algorithm was developed in Dr. Feld's group at MIT by several researches (29-31). This model based approach recovers not only the spectral shape but also the true fluorescence intensity, thus underlying fluorophore concentration can be quantified. Biswal *et at* proposed to utilize the polarized light fluorescence to reduce the absorption effects under the assumption that only the photons from superficial tissue maintain the original polarization (32). This approach is equivalent to limiting the imaging depth.

In this dissertation, we investigated wide field attenuation correction in fluorescence imaging utilizing SFDI imaging. Both optical property mapping capability and depth controlled imaging were employed in model based correction method and experimental method, respectively.

1.2.5.2 Polarized light SFDI imaging for soft tissue fibrous structure mapping

Many types of tissues are high dynamic, and its function is determined by the tissue structures. For example, the aortic heart valve withstands 30-40 million cycles per year. Studying the tissue structure properties, such as collagen fiber orientation, will facilitate better understanding of structure-function relationship, which may further lead to more advanced tissue engineering. One approach to study such relationship is performing constitutive model simulation (33). It has shown that by incorporating collagen fiber orientation into the model, the tissue response can be better predicted.

The availability and accuracy of fiber orientation currently limit the model development. Small angle light scattering or SALS (34) is the most widely used technology in quantifying the fiber orientation. However SALS imaging requires optical clearing to reduce the scattering of the sample which is destructive to the sample. Furthermore, SALS imaging uses raster scanning to cover the entire sample, which takes very long time. Together, it is challenging for SALS to obtain fiber reorientation of the sample under dynamic deformation. SALS imaging is a transmission based technique, thus it can only provide through- thickness averaged quantity. It potentially is a source of error for multi-layered samples.

By integrating the polarized light imaging (PLI) and SFDI imaging, more accurate fiber orientation mapping can be achieved. Polarized light in sensitive to fiber structures. Depending on the relative orientation between illumination polarization and the local fiber structures, the fiber structures scatter light differently, which provides a way to determine

the local fiber orientation. With SFDI imaging at high spatial frequency, the imaging depth is limited to the superficial layer. Thus, instead of through-thickness quantification, fiber orientation of the superficial layer can be accurately mapped.

1.2 DISSERTATION OVERVIEW

In Chapter 2, we present a hybrid LUT generation method, which uses MC simulation to generate an initial LUT and then it is scaled using a set of calibration phantoms. The LUT generated using this method is accurate and cost effective. In Chapter 3, we present two techniques to reduce the attenuation in fluorescence imaging. We first employ a model based method which utilizes tissue optical properties to compensate for attenuation. We also reduced absorption by limiting the imaging depth using structured illumination at high spatial frequency. In Chapter 4, we introduce an imaging technique combining polarized light imaging and SFDI imaging to accurately quantify collagen fiber orientation of the superficial layer of a heart valve leaflet. In Chapter 5, we develop a handheld SFDI imaging system for clinical skin characterization. Comprehensive skin properties are extracted, including optical properties, biochromophore concentration, fluorescence and color modulated reflectance image. Chapter 6 concludes the thesis, with future directions of our works.

CHAPTER 2 : MONTE CARLO SIMULATION BASED LOOKUP-TABLE METHOD FOR OPTICAL PROPERTIES MAPPING

2.1 INTRODUCTION

Methods of extracting optical properties in SFDI imaging have evolved over several phases. Initially, the method was developed for scattering dominant medium using standard diffusion approximation (SDA) (35).This method requires performing SFDI imaging at several spatial frequencies. The optical properties can be extracted by fitting the modulated reflectance to the diffusion model. The limitation of this method is apparent as it only works on scattering dominant samples, which requires sample to be low in absorption and high in scattering. The accuracy of this SDA based method is compromised when $(\mu_s^{'} / \mu_a) < 8$ (23). In biological tissues, this requirement typically can be met using NIR illumination. However, in visible range, most biological tissue can't be treated as scattering dominant media. The absorption in visible range is strong and is mainly from hemoglobin and melanin, especially the Q-bands between 540 and 576nm for hemoglobin absorption, at which $(\mu_s^{'} / \mu_a)$ could approach unity (36). Thus Erickson *et al* developed an experimental method that used tissue mimicking phantom system to generate look-up table (LUT), which can be used for tissue optical property extraction in visible range (21). An experiment based LUT is typically generated using an imaging system that will be later used for imaging on samples with unknown optical properties. Thus, the light delivery and detection geometry remains the same, which improves the quantification accuracy by accounting for system

specific properties. However LUT generation using experimental methods involves practical problems which may outweigh the benefits brought by this method.

The first issue of experimental LUT is the cost. To accurately control the scattering properties of the tissue mimicking phantoms, polystyrene microspheres are typically used. The scattering property of the microspheres then can be accurately predicted by Mie theory. However, the polystyrene microspheres are very expensive. Given the cost of microspheres, a typical phantom system can easily be over $1000. Furthermore, for each newly built system, a LUT needs to be generated, which makes this method even less economic. Lastly, it is inevitable to introduce error during the phantom making, especially a phantom system can have over 100 individual phantoms; thus the accuracy of LUT will be comprised.

To maintain the optical property coverage of LUT while reducing the cost, computational approach is more attractive. The key to generate LUT is to simulate the modulated reflectance. Multiple simulation strategies have been reported. Cuccia *et al* first described the method to simulate modulated reflectance by taking the Fourier transform of the impulse response of the turbid medium obtained using Monte Carlo (MC) simulation (16). More recently, analytical solutions to reflectance in spatial frequency domain were described (20, 33). Although analytical solutions are less computationally intensive, they can only simulate monolayer sample. MC simulation based method requires more computational power, however, its capability of handling multiple layers makes it more attractive and more versatile in SFDI study.

In biophotonics community, MCML program (37) is widely used to study light-tissue interaction in multi-layered samples. However, this program was created over 20 years ago and it was not optimized for current hardware. Recently, an updated graphic processing unit (GPU) based MCML program 'GPUMCML' was reported (38) to take advantage of parallel computing capability of modern GPU. GPUMCML can significantly reduce simulation time. GPUMCML program can be obtained as a free software under GNU general public license.

In this chapter, we will describe a hybrid approach to generate Monte-Carlo based LUT (MCLUT) that has the speed and versatility of MC simulation while maintaining the accuracy of a phantom based LUT.

2.2 METHOD

2.2.1 MCLUT Generation

In this section, we will generate a MCLUT following the protocol that has been described in detail in (21). Instead of experimentally measuring the reflectance, the reflectance will be simulated. To obtain the modulated reflectance, we first used GPUMCML program to simulate the tissue impulse response $R_d(\rho)$, where ρ is radial distance. The impulse response was then Fourier transformed (FT) (35) to get the modulated reflectance. Because the $R_d(\rho)$ is a radially symmetric function, the 2-D Fourier transform can be reduced to 1-D Hankel transform, Eq. 1, of order zero (35):

$$R_d(k) = 2\pi \int \rho J_0(k\rho) R_d(\rho) d\rho \tag{1}$$

where $k = f/2\pi$, and $J_0(k\rho)$ is the zeroth-order Bessel function of the first kind. The discrete form of this transform can be written as

$$R_d(f) = 2\pi \sum_{i=1}^{n} \rho_i J_0(f\rho_i / 2\pi) R_d(\rho_i) \Delta\rho_i \quad (2)$$

where $\Delta\rho_i$ is the sampling interval of diffuse reflectance. Two quantities, reflectance *R* and modulation *M*, were formulated for the LUT generation:

$$R = R_d(0) * \alpha_r \quad (3)$$

$$M = \frac{R_d(f)}{R_d(0)} * \alpha_m \quad (4)$$

where $R_d(0)$ is the reflectance at 0 spatial frequency, and $R_d(f)$ is the reflectance at spatial frequency *f*; α_r and α_m are two scaling factors and initial values for these two are set to 1.

The definitions of the *R* and *M* are slightly different from the ones in (21). This is because, from the experimental approach, only intensity data can be obtained, which needs to be normalized to get the reflectance. In simulation, the reflectance can be simulated directly. *R* and *M* are functions of both μ_a and μ_s', and this relation can be represented in Eq. 5 and 6,

$$R = f_R(\mu_a, \mu_s') \quad (5)$$

$$M = f_M(\mu_a, \mu_s') \quad (6)$$

To generate LUT, this relationship was transform to Eq. 7 and 8 using the algorithm described in (21).

$$\mu_a = f_a(R, M) \quad (7)$$

$$\mu_s' = f_s(R, M) \quad (8)$$

Thus, optical properties of an unknown sample can be determined by measuring *R* and *M*. To generate a LUT that covers wide range of bio-relevant optical properties, we chose following combinations of absorption and scattering coefficients: μ_a = 0.001, 0.01, 0.033, 0.066, 0.1, 0.3, 0.5, 0.7, 0.9, 1.1mm^{-1} and μ_s' = 0.4, 0.7, 1, 1.3, 1.6, 1.9, 2.2, 2.8, 3.1, 3.4, 3.7, 4, 4.3mm^{-1}. A total of 130 phantoms will be simulated.

2.2.2 MCLUT Scaling Based on Calibration Phantom

In this session, we examined the accuracy of optical properties extraction of liquid phantoms using MCLUT. A set of 20 phantoms were fabricated with μ_s' =1.5, 2, 2.5, 3mm^{-1} and μ_a =0.01, 0.05, 0.1, 0.3, 0.5mm^{-1}. Polystyrene microspheres with 1 μm diameter were used as the scatterings and black India ink was used as absorber. The concentration of beads for each scattering value was calculated using Mie theory. To match the experiment requirement, the wavelength used in Mie calculation was 490nm. Phantoms were imaged under 490nm illumination with a spatial frequency *f*=0.2mm^{-1}. The raw images were then normalized to a 99% reflectance standard to obtain reflectance images, which also eliminates the illumination non-uniformity.

Because the light delivery-collection geometry in simulation may not match the one in experiment, we expected discrepancy between extracted optical properties using MCLUT and true optical properties. To make MCLUT more system specific and to reduce the discrepancy, scaling factors α_r and α_m are adjusted iteratively thus the MCLUT was more tailored for experimental setup. In each iteration, the relative error on optical properties were evaluated until it converged.

2.3 RESULTS

2.3.1 MC Based Reflectance Validation

The impulse response function was sampled to perform discrete Hankel transform. The impulse response has a very steep slope closer to the source, which makes it important to determine appropriate sampling step to faithfully represent the impulse response. To study how sampling size affected the accuracy of modulated reflectance, we tested three step sizes of 2 μm, 5 μm and 10 μm for a phantom with μ_s' =3mm^{-1} and μ_a =0.1mm^{-1}. The comparison of corresponding modulated reflectance were generated and compared to the one generated using Virtual Tissue Simulator (VTS). VTS is a tissue simulation package developed in University of California, Irvine, which is able to simulate a wide range of light-tissue interaction. We consider the modulated reflectance from VTS as a reference for the validation purpose. Please note, that VTS assumes that reflective index n for the surrounding medium is 1.4. Although this assumption is not biologically relevant, it was still used for validation purpose. The comparison is shown in Fig. 2.1. As can be seen from the figure, reflectance with larger step size deviates more from the expected reflectance and overestimate the reflectance, especially at f=0mm^{-1} . At 10um step size, the relative error is about 4.5%, while at 2um step size, the error is only 1%. Thus, simulation with a smaller step size yielded more accurate results. In this study, a step size of 1.5um was used.

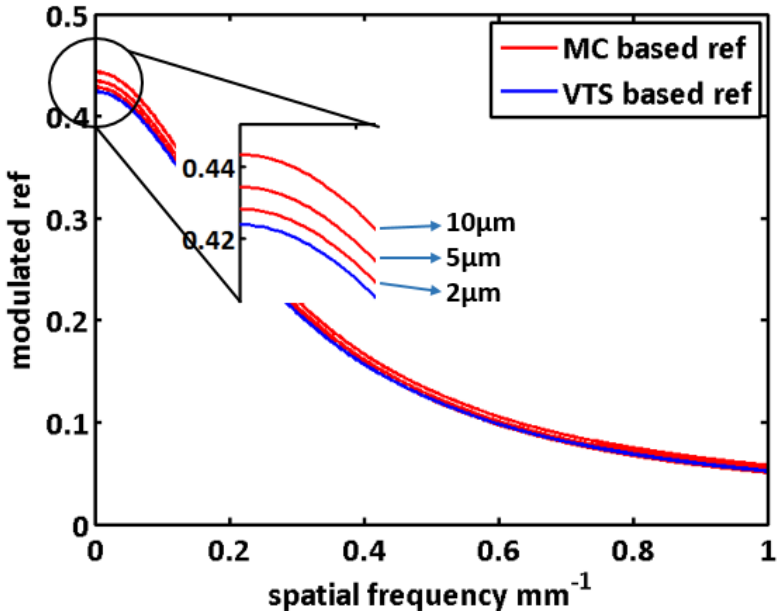

Figure 2.1 The effect of sampling step size on computed modulated reflectance. Modulated reflectance at three step sizes of 10, 5 and 2 µm was compared with the reference generated using VTS package

Before we generate the LUT using MC simulation based reflectance, we compared the reflectance obtained from MC-HT method to the reflectance from VTS solution for the validation purpose. The reflectance was simulated on a set of 9 phantoms with optical property combination with μ_s' =1, 2 and 3mm^{-1} and μ_a =0.01, 0.2 and 0.5mm^{-1}. The comparison was shown in Fig. 2.2. High degree of agreement can be observed over a large optical property range.

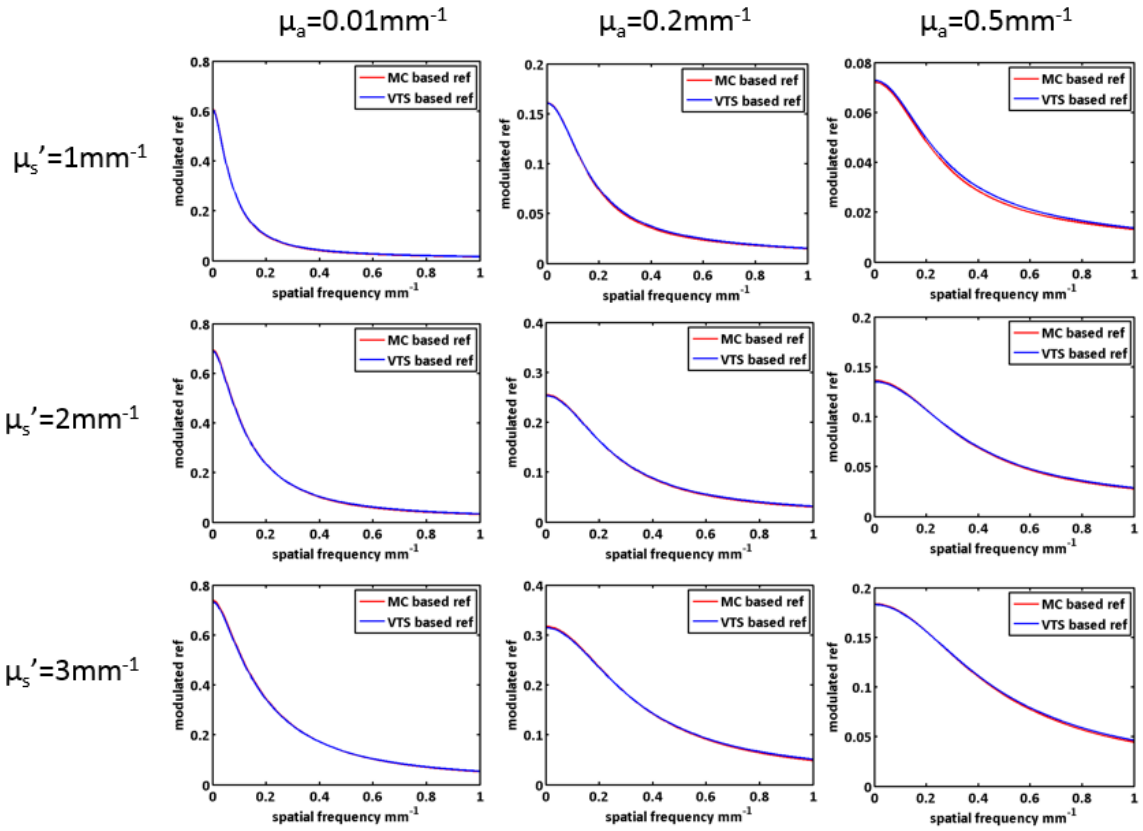

Figure 2.2 Comparison between the modulated reflectance generated using MC-HT method and the modulated reflectance generated using VTS package

2.3.2 Phantom Validation and Scaling

Optical properties of 20 phantoms were determined using MCLUT. Because the simulation does not represent real experimental setting, large error for both absorption coefficient and reduced scattering coefficient were observed. The average error for μ_s' is around -10%, however, the error for μ_a can be as high as 50%. We adjusted α_r and α_m iteratively, at each combination of α_r and α_m, the relative error was evaluated. We noticed when α_r=0.96 and α_m=0.97, the averaged relative error for μ_s' is about -7.5%, and for μ_a is about 2.3%. To further improve the accuracy, the extracted μ_s' was then scaled up by 6%, which resulted in

a decreased relative error of 3.25% for μ_s' quantification. Overall, by performing system calibration and scaling, the MC generated LUT can be applied to accurately extract optical properties for a specific imaging system.

2.4 CONCLUSION

In this chapter, we described a hybrid method to efficiently generate LUT that can be used to extract optical properties. The MCLUT is typically cost-efficient and accurate. However, pure simulation nature makes such LUT a generic one instead of an imaging system specific LUT. To make the MCLUT more imaging system specific, a MCLUT was calibrated and scaled using a set of phantoms with known optical properties. The phantoms were imaged and optical properties were extracted using MCLUT. By comparing the extracted and expected optical properties, the scaling factors during LUT generation were fine-tuned, which carried the imaging system characteristics. The optical properties extracted using calibrated and scaled MCLUT yielded an error of 2.3% for μ_a, and 3.25% for μ_s'. This method significantly reduces the both time and monetary cost of generating LUT while still maintaining imaging system specific accuracy.

CHAPTER 3 : ATTENUATION CORRECTED FLUORESCENCE IMAING USING SFDI[1]

3.1 INTRODUCTION

Fluorescence imaging of tissues is currently used in a number of clinical applications including identification of epithelia cancers, localization of solid tumors, and the resection of lymph nodes(39). Autofluorescence imaging highlights the biochemical properties of surface epithelial cancers for visualization and non-invasive diagnosis (10, 40, 41). Increasing or decreasing in fluorescence intensity may correlate with the health of the tissue, such as skin and oral cancers (42-45). The cancerous tissue typically display both morphologic and biochemical alternation, which results in local optical property changes. It has been reported that the red fluorescence is increased due to increased porphyrins concentration and green fluorescence in reduced due to breakdown of collagen cross links (46-48). On the other hand, exogenous fluorescence is typically obtained from fluorescent contrast agent either locally or systematically delivered. The bio-conjugated fluorescent contrast agent targets and accumulates in the region of interest (26). Different hallmarks of cancers can be used to target tumors (49). Over expression of signaling receptors such as EGFR and HER2 can be targeted using receptor-specific antibody. Targeting integrin alpha-v-beta-3 integrin can help visualize angiogenesis in the tumor. Under the excitation,

[1] This chapter was based on two published articles: 1) Yang, Bin, Manu Sharma, and James W. Tunnell. "Attenuation-corrected fluorescence extraction for image-guided surgery in spatial frequency domain." *Journal of biomedical optics* 18.8 (2013): 080503-080503. 2) Yang, Bin, and James W. Tunnell. "Real-time absorption reduced surface fluorescence imaging." *Journal of biomedical optics* 19.9 (2014): 090505-090505. The co-authors listed in these publications directed and supervised research which forms the basis for this chapter.

the fluorescence highlights the targeted region. This technique has showed the potential in solid tumor localization and identification. By identifying the tumor margin, the tumor could be removed more completely without leaving residual tumor, which will greatly improve the prognoses and reduce the recurrence rate. Indeed, molecular fluorescence based image-guided surgery will play an increasingly important role in the future of surgery

One challenge in fluorescence imaging is from strong tissue absorption and scattering, which complicates the identification and interpretation of the fluorescence signal. The region with high fluorophore concentration may be also be high in absorption, which could lead to very low fluorescence. In contrast, the region with low fluorophore concentration and low absorption may have even higher fluorescence. In the case of molecular fluorescence image-guided surgery, discrimination between fluorescently labeled tissues and that of normal or non-labeled tissues will be challenging. So it is desirable to obtain the fluorescence intensity representing the true fluorophore concentration. To compensate for the tissue attenuation, many techniques have been developed. The simple ratio methods developed by Kramer et al utilized the ratio of fluorescence intensity to backscattered excitation light intensity to compensate attenuation(50). Kramer et al also suggested by measuring fluorescence at two wavelengths, the changes in blood volume and oxygenation can also be corrected (50). More complex model based methods were developed try to achieve better attenuation correction capability These model based methods utilized different theories, such as using modified-Beer-Lambert law, Kubelka-Munk theory and photon migration theory (29, 30, 51, 52). However, most of these techniques are for the spectral correction of a point fluorescence measurement. The wide field attenuation

correction applications are very limited. Partly because the evaluation of the optical properties on either excitation or emission wavelength or both are necessary in order to perform robust correction using appropriate correction model. Such wide-field quantification was challenging before SFDI imaging was invented. Besides model based correction, the attenuation can also be reduced by reducing the imaging depth. It was reported that by introducing cross polarizers in fluorescence imaging, the imaging depth was limited by rejecting the depolarized light from deeper sample (32); thus, the absorption effects was reduced.

To explore the attenuation correction in fluorescence imaging using SFDI imaging technique, we conducted the study by using both model based correction and by physically limiting the imaging depth. Here, we will first present a novel technique to image tissue fluorescence free from the distortions of tissue scattering and absorption, called attenuation corrected fluorescence imaging (ACFi). ACFi combines techniques developed for single point (e.g. sensing) extraction of corrected fluorescence (30) and applies it to a whole image using spatial frequency domain imaging (SFDI) (21, 35). We adopted photon migration based correction method which was initially developed for point fluorescence correction(30). By performing wide-field optical properties mapping using SFDI imaging, we extended this method to image based measurements. The initial results showed that the attenuation can be recovered to within 10% variation compared to over 80% attenuation at highest biological relevant absorption. While these corrections are robust, lengthy data acquisition and processing can limit their usefulness in real-time imaging. Recently, a real-time imaging technique with absorption correction was reported which corrects the

absorption by normalizing the fluorescence image to a reflectance image at the excitation wavelength using two cameras (13). Here, we will demonstrate an absorption reduced surface fluorescence imaging (ARSFi) technique using spatial frequency domain imaging (SFDI) (16) that allows for real-time image rendering. We implemented SFDI at high spatial frequency to physically limit the imaging depth, thus reducing the absorption effects. We show that minimal computational processing is needed to render an ARSFi image, thus leading to a fast imaging speed of up to 19 frames per second using only one camera. In this chapter, these two techniques will be discussed in detail.

3.2 ATTENUATION CORRECTED FLUORESCECE EXTRACTON FOR IMAGING-GUIDED SURGERY IN SPATIAL FREQUENCY DOMAIN

3.2.1 Theoretical Background

The absorption and scattering attenuate the fluorescent signal at both excitation and emission wavelengths. To retrieve true fluorescence image, the attenuation at these two wavelengths needs to be compensated. We started with an attenuation correction model develop by Zhang et al (30). This model is based on photon migration theory, and is able to perform correction over a wide emission range from 370nm to 700nm. This model is summarized in Eq. 9,

$$f_{xm} = \frac{F_{xm}}{\frac{1}{\mu_{sx} l}\left(\frac{R_{0x}R_{0m}}{\varepsilon_x \varepsilon_m}\right)^{1/2} \frac{R_x}{R_{0x}}\left(\frac{R_m}{R_{0m}} + \varepsilon_m\right)} \tag{9}$$

where $\varepsilon = \exp(\beta) - 1$ and $\beta = S(1-g)$; F_{xm} is the raw fluorescence ; R and R_0 represent diffusive reflectance with and without absorption respectively; S and l are geometry

specific parameters; g is the anisotropy and μ_{sx} is the scattering coefficient of the sample at the excitation wavelength. Subscripts m and x denote reflectance at the emission and excitation wavelengths. Only F_{xm} and R_m were measured directly, while the other parameters were calculated analytically using the diffuse reflectance $R(\mu_a, \mu_s, g)$ of Zonios et al (53). The sample optical properties were determined by applying the same analytical model in an inverse fashion. This approach is able to recover not only the shape of the spectrum but also the absolute intensity of the spectrum. Note that in order to apply the correction of Eq. (9), one must directly measure the fluorescence F_{xm}, the reflectance R, and the optical properties in order to determine the corrected fluorescence.

This model is based on photon migration theory and this theory describes the photon propagation in turbid medium, including absorption, scattering and fluorescence. The photon behavior is independent on illumination and detection techniques, which means it can be applied to both point based measurements and image based measurements. Wu *et al* suggested that this method is valid as long as the light delivery and collection geometry remain the same(31). One thing need to be noted is that the signal detected at each pixel has the convolved contributions from its neighboring sources, which is different from the point measurement. This particular geometry is accounted for by the parameter *S*.

Applying this model to wide field measurement, we used the SFDI imaging to quantify the optical properties, μ_a and μ_s' at both excitation and emission wavelengths. The μ_a and μ_s' were obtained using a look-up table (LUT) method(21). The reflectance at excitation wavelength R_x and fluorescence image Fxm were imaged with and without filter,

respectively. In order to obtain reflectance without absorption R_{0x} and R_{0m}, the μ_a was set to 0, thus by using LUT in a forward manner, the reflectance without reflectance can be retrieved. The system specific values S was determined using calibration phantom. Since relative fluorescence does not depend on system constant l, thus l was not determined.

3.2.2 Experimental Setup and Data Collection

We developed an ACF imaging system to perform both fluorescence imaging and SFDI imaging. The system schematic is shown in Fig. 3.1. A 2-D spatially modulated sinusoidal pattern is generated on a digital micromirror device (DMD) (Discovery 1100, TI) and the diffusively reflected images are captured with a non-cooled CCD camera (Allied Vision, F145B). By projecting patterns with the same spatial frequency but phase offsets at 0, $2\pi/3$ and $4\pi/3$, three separate images with diffusively reflected intensities of I_1, I_2 and I_3 respectively, can be used to calculate the AC and DC components. The illumination area is about 3cm x 4cm. In the imaging system, we used both 365nm and 490nm LED as excitation light source for in-vitro and ex-vivo experiments. And a 530nm LED was used for the fluorescence imaging at emission wavelength. In the in-vitro phantom study, the phantom was excited at 365nm with a UV LED (Thorlabs, M365L2) and peak emission occurred at approximately 520nm. Two bandpass filters with central wavelengths of 520nm and 530nm were used during the data acquisition under 365nm and 530nm illumination, respectively, in order to collect fluorescence F_{xm} and the reflectance at the emission R_m. A low-pass filter with a 420nm cut-off was used to isolate the diffuse reflectance under illumination at the excitation wavelength. In the ex-vivo tissue study, we

chose a 490nm LED as the excitation source to better suppress the autofluorescence and match the excitation wavelength that may be used in a clinical setting. A 500nm low-pass filter was used to collect the diffuse reflectance from the excitation. All results in this letter were obtained using a 40% reflectance spectralon to normalize the signal and to correct for non-uniformities in the illumination field.

The spatial frequency used in our study was $0.1mm^{-1}$. Our previous study(21) showed that at this spatial frequency, the optical properties of the sample can be extracted with RMS errors of 5.7 and 2.9% for μ_s' and μ_a, respectively.

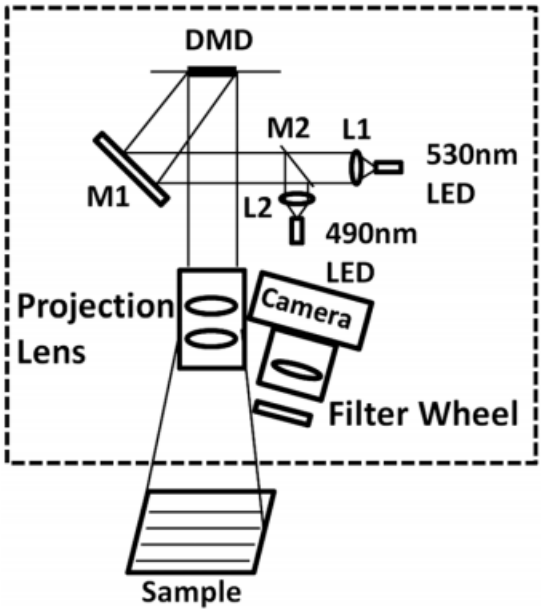

Figure 3.1 Optical layout of ACF imaging system. Patterns are generated on the DMD, illuminated by LEDs and projected by the projection lens to the sample. Filter wheel is used to select the wavelength and the imaging field is captured by a CCD camera

3.2.3 Sample preparation

We prepared sample for both in-vitro and ex-vivo experiment to examine the performance of this technique. In in-vitro experiment, we prepared tissue simulating liquid phantoms using black India in and 20% intralipid (Fresenius-Kabi) as absorber and scatterer, respectively. In this study, we used fluorescein (ACROS ORGANICS) as the fluorophore because of its high quantum yield and biological relevance(27). We designed the optical properties of the phantoms to be biologically relevant. A total 3 sets of 15 phantoms were fabricated. The reduced scattering coefficient μs' maintained constant for each set and the μs' was designed to be 1.0, 1.4 and 1.8 mm^{-1} at 530nm. In each set, the absorption coefficient was varied from 0.05mm^{-1} to 0.45mm^{-1} with an increment of 0.1mm^{-1} at 530nm. The fluorescein concentration was keep the as for all phantoms at 6.5 μg/ml. The anisotropy of intralipid was estimated as 0.9 at 365nm and 0.85 at 530nm based on the model of Flock et al (54).

For ex vivo experiment, we designed a simplified tumor model using minced chicken breast tissue. The tissue phantom is about 8mm in thickness. The tumor was made using the same chicken breast tissue but was homogenously mixed with fluorescein solution and was embedded in the center of the tumor model. To introduce additional absorption, part of the tumor was covered with hemoglobin solution (SIGMA-ALDRICH, H0267) at a concentration of 10mg/ml. Thus, the contrast between normal tissue and tumor as well as the tumor with and without additional absorption can be demonstrated.

3.2.4 Results

The in vitro experiment results were shown in Fig. 3.2. Figure 3.2 shows the results from the experiment where all phantoms have the same fluorescence concentration (and thus the fluorescence intensity should remain the same). The phantoms without correction showed a substantial decrease in fluorescence intensity with increasing absorption for all scattering values, with a fluorescence intensity drop of more than 80% at the highest level of absorption. This intensity decrease is qualitatively appreciated in the top row of images in Fig. 3.2d. This attenuation was primarily due to strong absorption at both excitation and emission wavelength. Two correction techniques were applied (F/R and ACF). The anisotropy of intralipid was estimated as 0.9 at 365nm and 0.85 at 530nm based on the model of Flock et al (54). After applying the ACF correction algorithm, the highest variation of fluorescence intensity was reduced to 5.1%, 9.7% and 12% for the 3 phantoms sets, respectively. Thus, a much more uniform profile was recovered. The ACF correction out-performed the F/R technique over the entire range of optical properties. For the ACF correction, as scattering becomes more pronounced, the attenuation is increased. Fig. 3.2(d) is a 2D fluorescence image of the phantom set with $\mu_s' = 1.4mm^{-1}$ before and after ACF correction; significant improvement in the recovered fluorescence intensity is observed as all images maintain approximately the same intensity. The image quality (i.e. SNR) of the corrected images generally decreases with increasing absorption. This decrease in SNR can be understood qualitatively by recognizing the decrease in the image signal with increasing absorption. This noise issue will be investigated in future study.

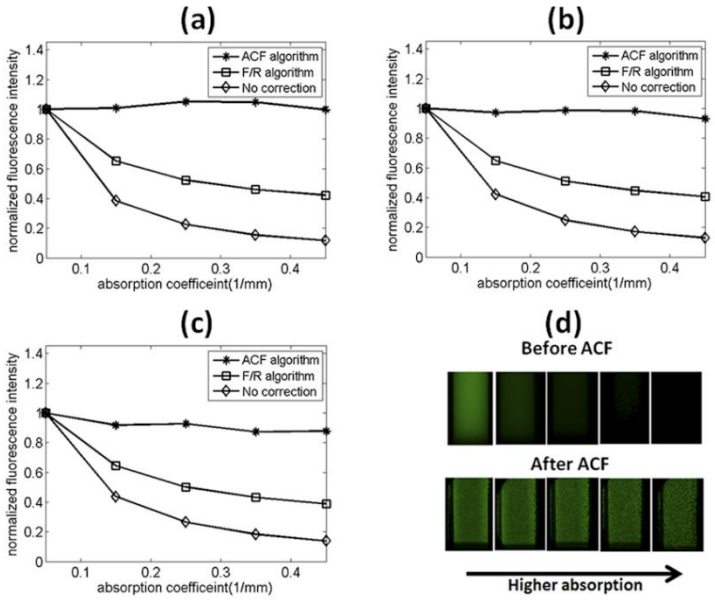

Figure 3.2 Normalized fluorescence intensity of in-vitro tissue phantom with ACF correction, F/R correction and no correction for three scattering values: (a) $\mu_s^{'} = 1.0mm^{-1}$, (b) $\mu_s^{'} = 1.4mm^{-1}$ and (c) $\mu_s^{'} = 1.8mm^{-1}$. (d) The 2D fluorescence images before and after the ACF correction for phantoms in (b).

For the ex vivo experiment, we first determined the anisotropy of the sample as 0.9 and 0.91 at 490nm and 530nm, respectively using Mie theory. Figure 3.3b shows that only half of the tumor is visible to the naked eye, and the margin of the lower portion of the tumor is poorly defined due to the presence of the blood. This is consistent with the raw fluorescence image, Fig. 3.3c. We can see that the upper-portion is bright, whereas the lower-portion, covered with blood, is dull in comparison, due to hemoglobin absorption at the excitation and emission wavelengths. Therefore, in practice, this could result in only half of the tumor being excised. The application of the correction algorithm, Fig. 3.3d, results in a marked improvement as the whole tumor is now visualized. Furthermore, the corrected image accurately recovers the tumor margin and the uniform fluorescence intensity distribution. Excellent contrast can be observed between the background and the signal. The ex-vivo results suggest that ACF is equally applicable to heterogeneous tissues and

is able to yield consistent results as seen in the in-vitro homogenous phantom study. For comparison purposes, Fig. 3.3e shows the result from the F/R ratio method. The attenuation is partially compensated by using the F/R ratio method; however, the intensity difference between the upper and lower portion of the tumor can still be observed. The black dots present in Fig. 3.3d and 3.3e are due to the specular reflection. Overall, these results are very promising as they indicate the potential of the ACF correction approach for image-guided surgery towards accurate identification of the entire tumor region.

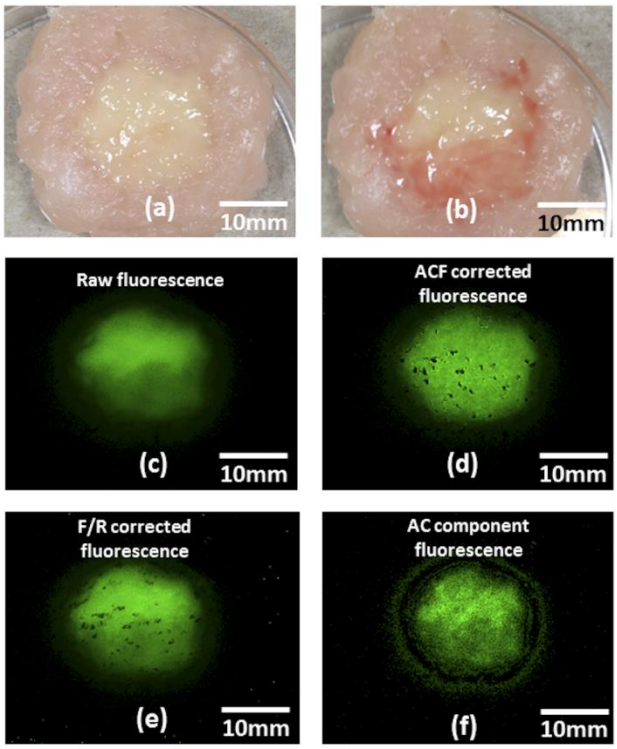

Figure 3.3 Color image of tumor model (a), the tumor model partially covered with the blood (b), intensity image of the raw fluorescence under 490nm illumination (c) and retrieved attenuation corrected fluorescence image (d) from the raw fluorescence, the corrected fluorescence (e) using F/R ratio method, and fluorescence image from AC component (f).

3.2.5 Discussion and conclusion

By taking advantage of the SFDI technique, we have demonstrated the efficacy of the attenuation corrected fluorescence extraction in an imaging field. Unlike other approaches, the performance is minimally affected by the underlying optical properties of the sample, and minimal knowledge of the sample optical property information is necessary to perform the correction. Although robust performance was achieved, there are three issues that should be noted. First, ACF is able to achieve the attenuation correction not because of optical sectioning, but because of the physical correction model used. The AC component image of the measurement obtained from optical sectioning (55), Fig. 3.3f, was demonstrated to be different from the ACF corrected fluorescence, Fig. 3.3d. Second, in our study, the samples are relatively flat, and no curvature correction algorithm (56) was employed. However, the curvature correction for SFDI has been described in the literature (56), and could be implemented for the purposes of ACF imaging in future applications. Third, note that the diffuse reflectance at the excitation wavelength R_x was measured directly by using a low pass filter. R_x is an estimate of the true value of the diffuse reflectance without fluorescence. With the presence of the fluorophore, the incident excitation light is partially absorbed by the fluorophore. The results from the tissue simulating phantom experiment indicated that the difference in diffuse reflectance with and without the fluorophore is less than 8% for a fluorophore concentration of $6.5\mu g/ml$. Therefore, the optical properties of the phantom at the excitation wavelength can still be estimated.

3.3 REAL-TIME ABSORPTION REDUCED SURFACE FLUORESCENCE IMAGING

3.3.1 Absorption reduction theory

To reduce the tissue absorption in fluorescence imaging, we chose to limit the imaging depth by using SFDI imaging at high spatial frequency. SFDI was first introduced for the quantitative evaluation of optical properties of a turbid medium using structured illumination (16). SFDI has a spatial frequency dependent sensitivity on both absorption and scattering (35). At high spatial frequency, SFDI has high sensitivity to scattering but low sensitivity to absorption. In a scattering dominant medium, the effective penetration depth $\delta_{eff}^{'}$ can be described in Eq. 10,

$$\delta_{eff}^{'} = (\sqrt{3\mu_a(\mu_a + \mu_s^{'}) + (2\pi f)^2})^{-1} \tag{10}$$

where μ_a and $\mu_s^{'}$ are the absorption coefficient and the reduced scattering coefficient, respectively, and f is the spatial frequency. At high spatial frequency, the penetration depth is mainly determined by spatial frequency. Thus Eq. 11 can be reduced as

$$\delta_{eff}^{'} = (2\pi f)^{-1} \tag{11}$$

Using high spatial frequency structured illumination, the imaging depth can be limited which results in reduced absorption in fluorescence imaging.

We obtained an absorption reduced fluorescence image by performing standard SFDI imaging and demodulating the fluorescence images at high spatial frequency. Three patterns with phase shifts of 0°, 120° and 240° were projected to the sample, and the

corresponding fluorescence image I_1, I_2 and I_3 were recorded. The DC and AC images were obtained from the demodulation shown in Eq. 12 and 13,

$$I_{dc} = 1/3(I_1 + I_2 + I_3) \tag{12}$$

$$I_{ac} = \sqrt{2}/3\left(\sqrt{(I_1 - I_2)^2 + (I_2 - I_3)^2 + (I_3 - I_1)^2}\right) \tag{13}$$

The DC image would be the same as if the sample was illuminated by a planar excitation. On the other hand, the AC image is spatial frequency dependent and is also considered the absorption reduced fluorescence image.

3.3.2 Imaging system development

We developed a custom video rate SFDI fluorescence imaging system to perform the real-time fluorescence visualization with absorption minimization. The LightCrafter evaluation module (LC-EVO, Texas Instruments) was used to generate and project patterns. Specifically, the LC-EVO worked in stored-pattern-sequence mode, which avoided the internal gamma correction. A non-cooled CCD camera (piA2400-17 gm/gc, Basler) with a fast lens (Fujinon, HF25HA-1B) was used for image acquisition. A 490nm LED low-pass filtered at 500nm was used for the excitation. A 510nm high-pass filter (BrightLine FF510, Semrock) was used for fluorescence collection. The light engine of the LC-EVO was custom modified, thus the minimal diagonal image size was reduced from 25.4cm to 2.8cm with 2cm working distance to achieve high intensity illumination and high spatial frequency pattern. The projection magnification and working distance can be adjusted to meet specific application requirements. In our study, the imaging area was 2.6cm by 1.6cm.

The challenge of achieving real-time imaging with SFDI is that the standard SFDI demodulation technique requires 3 frames of the reflectance image, which is generally slow and is a source of the motion artifacts. More advanced demodulation techniques require less frames; however, the image quality is compromised and requires more computational power (57, 58). To address this challenge, we optimized both image acquisition and image processing. To achieve fast image acquisition, we used a highly efficient fluorescence collection system. We used an imaging camera having over 60% quantum efficiency at the emission wavelength with a fast lens having F/1.4 large aperture. The fluorescence filter we used has over 93% transmission for wavelengths longer than 515nm. Together, we were able to achieve good SNR images with a 20ms integration time. To optimize the imaging processing, we adopted the following strategies: 1) utilize the cyclic projected patterns; 2) implement parallel threads and a 3-frame shared buffer for image acquisition and processing (Fig. 3.4). Because the patterns are cyclic, starting from the third frame, for every newly acquired frame plus two previously acquired frames, we can derive a processed image, which is equivalent to conventional video-rate imaging except the processed image has the 'three-frame-motion-memory'. We introduced parallel threads and a three-frame shared buffer to avoid asynchronization and competition between image acquisition and processing. The newly acquired image was pushed into the buffer and the oldest image in the buffer was then discarded. With the shared buffer, both image acquisition and image processing threads can be optimized individually without introducing interference between the two. Comparing this correction technique with model based techniques, the advantage is evident as this technique only requires one incremental

frame to derive one attenuation corrected image versus 9 frames for each attenuation corrected image using model based correction.

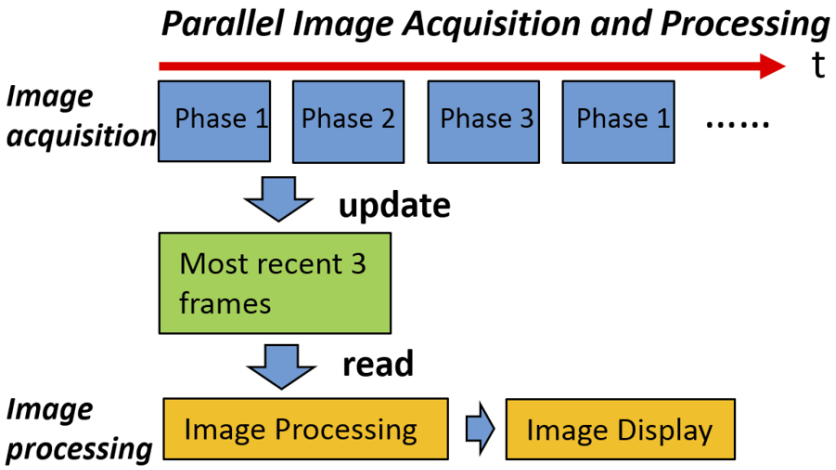

Figure 3.4 Block diagram of parallel image acquisition and processing. A shared buffer stores most recent 3 frames and connects image acquisition and processing processes

3.3.4 Phantom fabrication

To study the spatial frequency dependent performance of ARSFi, we imaged 5 tissue mimicking liquid phantoms at 4 spatial frequencies 0.5mm^{-1}, 0.35mm^{-1}, $0.2\ \text{mm}^{-1}$ and 0.1mm^{-1}. The phantoms were fabricated with constant reduced scattering coefficient of $\mu_s^{'} = 2.0\,\text{mm}^{-1}$ and constant fluorescein concentration at $15\mu g / ml$, while the absorption increased from $0.05 mm^{-1}$ to $0.45 mm^{-1}$ with an increment of $0.1 mm^{-1}$.

In the ex-vivo tissue study, minced turkey breast was homogenously mixed with fluorescein solution of a concentration of $0.18 mg / ml$. Half of the tissue was further mixed with black India ink with $\mu_a = 0.42 mm^{-1}$ to introduce additional absorption.

3.3.5 Results

The in vitro experiment results are shown in Fig 3.5. DC fluorescence experienced an approximately 70% drop in intensity at the highest absorption. On the other hand, the demodulated AC components were less affected by absorption at all spatial frequencies. Moreover, the absorption minimization performed better at higher spatial frequency.

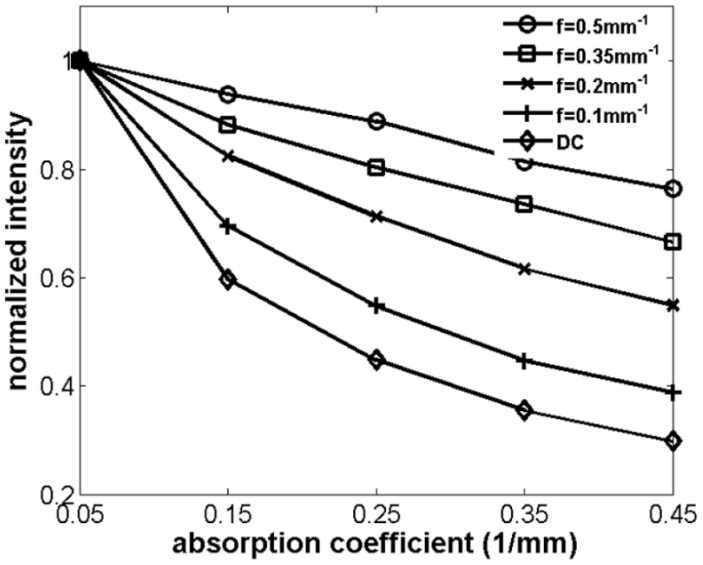

Figure 3.5 Normalized fluorescence intensity of DC and AC components retrieved from five tissue mimicking phantoms with absorption increasing from 0.05mm^{-1} to 0.45mm^{-1}

The raw fluorescence image showed the tissue with ink had much lower intensity than the tissue without ink in Fig. 3.6(b). The ARSFi image (Fig. 3.6(c)) showed a more uniform intensity distribution over the entire tissue. The cross-sectional plot (Fig. 3.6(d)) suggested the ink was responsible for an approximately 50% intensity drop in the raw fluorescence image, while only around 10% in AC image. Furthermore, in AC image, an enhanced resolution and contrast can also be observed. This spatial frequency based enhancement is consistent with previous report (55). It needs to be noted that the dark zones in Fig. 3.6(c)

suggest less fluorophore was distributed in those surface regions, which does not necessarily mean the absence of fluorophore located beneath the dark regions.

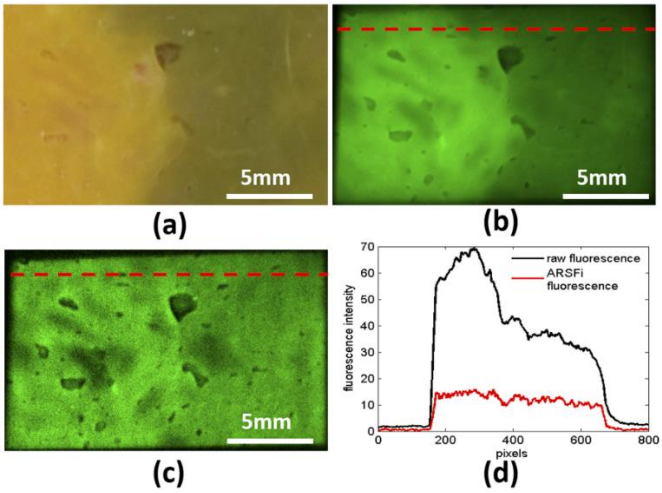

Figure 3.6 Color image of ex-vivo tissue model (a), raw fluorescence image (b), high spatial frequency fluorescence (c) and cross-sectional plot (d).

Although good absorption minimization can be achieved, ARSFi is a surface fluorescence imaging technique. We conducted the depth analysis to show the depth imaging properties of ARSFi. A fluorescent phantom with μ_a=0.05mm^{-1} and μ_s'=2mm^{-1} was embedded in a media with μ_a=0.15mm^{-1} and μ_s'=1mm^{-1}. The phantom was gradually translated 300 μm into the media with a step size of 50 μm. At the each depth, the phantom was imaged at f=0.5mm^{-1}. The result (Fig. 3.7) shows that AC signal dropped rapidly as the phantom went deeper into media. The fluorescence was marginally detectable when the sample was embedded ~300 μm into the media, which is close to the 330 μm imaging depth suggested by Eq. 3. This technique may not be suitable for certain image-guided surgery applications where the targeted tumor is deeply embedded in the tissue. Furthermore, while this study addresses the imaging system, we note that image-guided surgery is a multifaceted problem

dependent as well on the fluorescent contrast agent development, delivery and visualization. However, such a technique would be suitable for surface imaging applications such as tumor margin detection and epithelial tumor imaging.

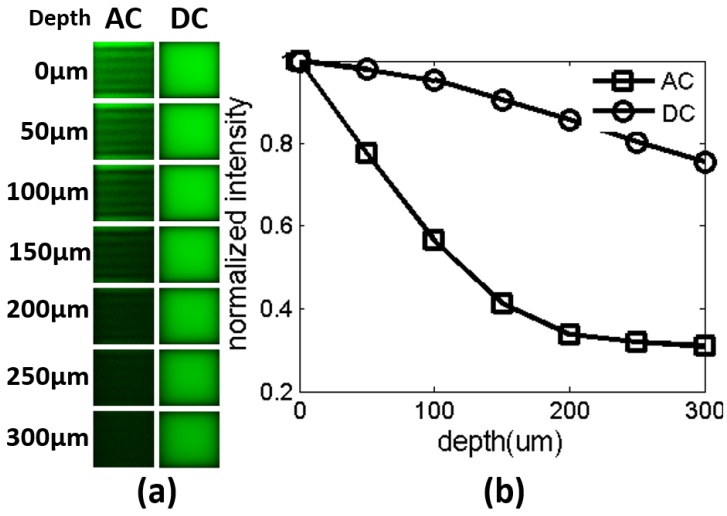

Figure 3.7 AC and DC fluorescence intensity at 7 depths. (b) Normalized AC and DC intensity plot at 7 depths

The real-time ARSFi system is able to perform raw image acquisition at 20 frames/second. The demodulated image can be displayed at around 19 frames/second. Although the exposure was only 20ms, the image read-out time currently limited the frame rate of the image acquisition. The motion memory in the current imaging system is around 150ms, which means that the demodulated image is a temporal average over 150ms time period. It further suggests that 150ms after the motion stops, the demodulated image will become stable. The typical motion artifact in real-time ARSFi is shown in Fig. 3.8. Without the motion, the demodulated image Fig. 3.8a faithfully represents the imaging field. In the presence of the motion, a ghost image can be observed in Fig. 3.8b. The faster the motion,

the more significant the motion artifact. The motion artifacts can be greatly reduced with a fast video camera.

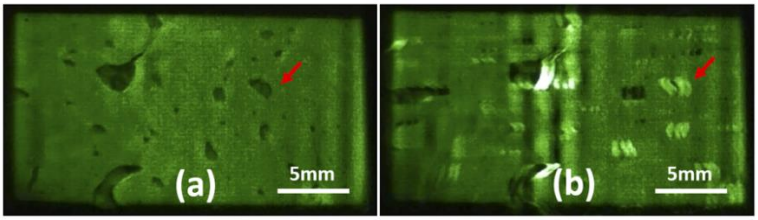

Figure 3.8 Demodulated fluorescence image without motion (a) and with motion (b) (Video1). The red arrow indicates the demodulated feature. With the motion, the ghost image can be observed

3.3.6 Conclusion

In this section, we presented a novel approach to reduce the absorption effects in fluorescence imaging by using SFDI at high spatial frequency. While the real-time ARSFi technique is not as robust as other model based techniques, it provides the ability for video rate imaging. The real-time implementation of ARSFi suggests that this technique has potential in tumor margin detection and cancer visualization.

3.4 CONCLUSION

In this chapter, we described 2 methods that compensate the tissue attenuation in fluorescence imaging. ACFi performs robust attenuation correction by evaluating tissue optical properties and using a photon migration based correction method. The fluorescence intensity attenuation is within 10% after correction compared over 80% drop in raw fluorescence intensity for both *in-vitro* phantom and *ex-vivo* tissue studies. Although robust, ACFi needs to evaluate optical properties at both excitation and emission wavelength as well collecting raw fluorescence images. This lengthy imaging and data processing make

it ideal for static sample imaging, such as excised tissues, instead of real-time resection guidance. To achieve real-time attenuation correction, we developed ARSFi which utilized depth controlled imaging capability of SFDI imaging. Imaging at high spatial frequency, only the superficial layer is imaged; thus attenuation especially the absorption at both excitation and emission is greatly reduced, which permits imaged fluorescence reflecting fluorophore concentration regardless of local absorption property. Image processing for ARSFi requires minimal computational power, thus, real-time rendering is possible. We achieved 19 frames/second for ARSFi. At this frame rate, it is possible to study epithelial cancers such as oral and skin cancer and tumor margin detection in real-time. ARSFi can be integrated with high spatial frequency reflectance imaging to study scattering properties with minimal absorption interference.

CHAPTER 4 : POLARIZED LIGHT SPATIAL FREQUENCY DOMAIN IMAGING FOR NON-DESTRUCTIVE QUANTIFICATION OF SOFT TISSUE FIBROUS STRUCTURES[2]

4.1 INTRODUCTION

Many types of soft biological tissues primarily consist of aligned fibrous structures (59, 60). The anisotropic fiber organization in soft tissues results in distinct mechanical properties and functions, directed towards optimal physiological function. Fully understanding these structure-function relationships and integrating this knowledge into predictions of the resulting tissue behavior remains an ongoing challenge for a wide range of tissue applications(61). Directly incorporating fiber orientation information within soft tissue models better predicts their mechanical response (62).

A variety of imaging approaches have been developed to retrieve structural information based on the scattering and birefringent properties from aligned structures at both organ level (34, 63-66) and microscopic level (10, 67, 68). For example, small angle light scattering (SALS) has been used extensively in soft tissue analysis(34). SALS has an advantage of directly quantifying the angular distribution of fibers rapidly and over large areas of tissue. However, it is a transmitted light technique and remains limited to either thin sections or tissue that have undergone some type of optical clearing (e.g. glycerol

[2] This chapter was based on the published article: Yang, Bin, John Lesicko, Manu Sharma, Michael Hill, Michael S. Sacks, and James W. Tunnell. "Polarized light spatial frequency domain imaging for non-destructive quantification of soft tissue fibrous structures." *Biomedical optics express* 6, no. 4 (2015): 1520-1533. John, Dr. Sharma and Dr. Hill contributed to experiment part. Dr. Tunnell and Dr. Sacks supervised the research.

immersion). Moreover, transmural variations are lost as the resulting scattering patterns represent the through thickness average(11). Microscopic fiber orientation imaging techniques typically have challenges for large sample imaging. Polarization-sensitive optical coherence tomography (OCT) has demonstrated its capability of extracting fiber orientation (66). More recently, Konecky *et al* reported a technique using rotating spatial patterns to rapidly measure scattering orientation index(SOI) (69). The typical challenge in tissue imaging arises from strong tissue scattering (70). For transmission-based techniques, to reduce this scattering, the sample is normally thinly sectioned or chemically cleared (34, 64), which is destructive to the sample. In reflection-based imaging, cross-polarization gating is utilized to suppress diffuse photons (71). Furthermore, many types of tissues are heterogeneous in structure through their depth. Without proper depth imaging capability, the acquired signal may be averaged over the depth which adversely affects the layer specificity of the measurement.

Here we report a novel wide –field imaging technique that combines polarized light imaging (PLI) with spatial frequency domain imaging (SFDI) at high spatial frequency (16) to determine the local fiber orientation on native tissues, which we term polarized light SFDI (pSFDI). In this integrated imaging technique, PLI utilizes the polarization dependent scattering property of fibers to determine the fiber orientation, and SFDI imaging at high spatial frequency is introduced to reject the highly diffuse photons and to control the imaging depth. As a result, the photons from the superficial layer of a multi-layered sample are highlighted, thus we can achieve more accurate fiber orientation quantification for the

superficial layer. Furthermore, pSFDI is able to perform imaging on native tissue with minimal preparation and without the need for chemical treatment.

4.2 METHODS AND INSTUMENTATION

4.2.1 Cylinder Scattering Simulation

Highly aligned fibrous structures exhibit strong polarization dependent light scattering properties. As a first order approximation, we modeled light scattering fibrous tissues as individual, infinitely long dielectric cylinders. For clarity, a single collagen fiber and scattering cylinder can be thought of as interchangeable terms in this paper. The theory of polarization dependent scattering by cylinders has been thoroughly described (72, 73). The back-scattered light from a cylinder depends on both the incident light's in-plane polarization angle and the cylinder's orientation.

We developed a rotating polarization imaging model to study the properties of the light back-scattered from collagen fibers. Fig. 4.1 depicts the simulation geometry. Fibers of varying diameters align in the x-z plane at 30 degree with respect to x axis. Linear polarized incident light traveling in the y direction illuminates the fibers at normal incidence, and linearly polarized backscattered light is collected at the same polar angle. In other words, the illumination and the collection are co-polarized; thus, only the photons with the same polarization as the incident photons are collected. The incident light (and collected light) polarization angle θ varies from 0 to 180 degrees anticlockwise with respect to the x-z plane.

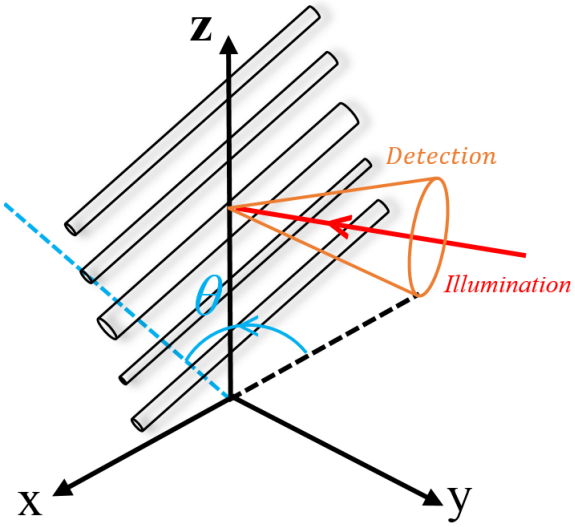

Figure 4.1 Cylinder light scattering simulation geometry. The cylinders orient at 30 degree with respect to x axis. The polarized light illuminates a collection of cylinders with multiple diameters at normal incidence. The polarization angle θ of the incident light rotates anti-clockwise from 0 degree to 180 degrees

The back-scattered light can be analytically described using Mueller calculus by summing the scattered light from all fibers, shown in Eq. 14 as

$$S_{out}(\theta) = \sum_{scat=1}^{n} M_{pol} M_{rot}(-\theta) M_{scat} M_{rot}(\theta) M_{pol} S_{in} \tag{14}$$

where,

$$M_{scat} = \sum_{\varphi=-\varphi_{col}}^{\varphi=\varphi_{col}} \begin{bmatrix} M_{11}(\varphi) & M_{12}(\varphi) & 0 & 0 \\ M_{12}(\varphi) & M_{11}(\varphi) & 0 & 0 \\ 0 & 0 & M_{33}(\varphi) & M_{34}(\varphi) \\ 0 & 0 & -M_{34}(\varphi) & M_{33}(\varphi) \end{bmatrix} \tag{15}$$

$$M_{pol} = \begin{bmatrix} 1 & 1 & 0 & 0 \\ 1 & 1 & 0 & 0 \\ 0 & 0 & 0 & 0 \\ 0 & 0 & 0 & 0 \end{bmatrix} \tag{16}$$

$$M_{rot}(\theta)=\begin{bmatrix}1 & 0 & 0 & 0\\ 0 & \cos(2\theta) & \sin(2\theta) & 0\\ 0 & -\sin(2\theta) & \cos(2\theta) & 0\\ 0 & 0 & 0 & 1\end{bmatrix} \quad (17)$$

$$S_{in}=\left[I_{in},Q_{in},U_{in},V_{in}\right]^{T} \quad (18)$$

$$S_{out}=\left[I_{out},Q_{out},U_{out},V_{out}\right]^{T} \quad (19)$$

M_{scat} is the scattering matrix that describes the back scattering property of cylinders and the back scattering efficiency was summed over an angular range of [$-\varphi_{col}$, φ_{col}] during the construction of M_{scat}. The detailed derivation of the elements of scattering matrix M_{scat} can be found in the classic light scattering books (72, 73). M_{pol} and M_{rot} are matrices representing the linear polarizer and rotator, respectively. Stokes vectors S_{in} and S_{out} describe the polarization state of the incident light and the scattered light, respectively. I,Q ,U and V are the four elements of a Stokes vector with I representing the detected intensity. The incident light is unpolarized; thus, S_{in} is reduced to $S_{in}=[1,0,0,0]^{T}$. S_{out} is calculated at each polarization angle θ. In our study, only the back-scattered light intensity I_{out} in S_{out} was examined.

We simulated cylindrical light scattering to establish the relationship between the collected polarized light signal and the fiber orientation, which led to the method for determining local fiber orientation. In the simulation, fibers with refractive index of 1.48 were modeled in a medium of refractive index of 1.33. The fibers were oriented at 30 degree with respect to x-axis. The illumination wavelength was 490nm with normal incidence. The polarization of the illumination was rotated through 180 degrees in one degree increment. The back-scattered light was then detected.

For real tissues, the collagen fibers are rarely all aligned to a single orientation. A distribution of fiber alignment is expected. To study the effects of local fiber distribution, we performed the same simulation over a collection of fibers with fiber orientation following a normal distribution. The preferred orientation or mean orientation was still at 30 degrees. The standard deviation of the fiber orientation varied from 0 degree to 20 degrees with an increment of 5 degrees. We also simulated the scattering property on fibers with totally random orientations. The overall scattering property was simulated on 3000 fibers.

4.2.2 SFDI Imaging and Diffuse Background Rejection

As photons propagate deeper into the tissue, they typically will 1) become highly diffusive through multiple scattering events and 2) interact with structurally distinct layers in multilayered samples. Both effects will either mask or distort the back-scattered photons from the superficial layer. Utilizing SFDI imaging at high spatial frequency allows for the rejection of these diffuse photons and enhancement of the information from the superficial layer. SFDI imaging is an effective tool for quantitative evaluation of tissue optical properties over a wide field of view (35). In SFDI imaging, three phase-shifted sinusoidal illumination patterns are projected onto the sample. We collect diffuse reflectance images containing pattern-tissue interaction in order to retrieve sample optical properties. Besides optical property mapping, SFDI imaging can also perform depth controlled imaging by varying the spatial frequency. The penetration depth in SFDI imaging is determined by both optical properties (absorption and scattering) and spatial frequency. As the illumination pattern propagates into the medium, the modulation of spatial pattern becomes

attenuated due to scattering and absorption. The modulation or AC image was extracted using demodulation technique shown in Eq. 13, where I_1, I_2 and I_3 are the reflectance images of the sample under three sinusoidal illumination patterns with phase shifts of 0^o, 120^o and 240^o,respectively (16). Higher the spatial frequency is, faster modulation attenuation will be. Thus, the turbid medium acts like a low-pass filter. For high spatial frequency pattern, the modulation can only be preserved at very shallow depth. The effective penetration depth δ'_{eff} depends on both the tissue optical properties and the spatial frequency of the illumination pattern. The effective penetration depth for a scattering dominant medium can be described using Eq. 10 (35)

$$\delta'_{eff} = (\sqrt{3\mu_a(\mu_a + \mu_s') + (2\pi f)^2})^{-1} \tag{10}$$

where μ_a is the absorption coefficient, μ_s' is the reduced scattering coefficient and f is the spatial frequency. At high spatial frequency, the effective penetration depth mainly depends on the spatial frequency, and thus can be approximated as

$$\delta'_{eff} \approx (2\pi f)^{-1} \tag{11}$$

This suggests that the penetration will be nearly constant across the entire sample and has weak dependency on sample optical properties. Thus sample wide penetration variation will be very small. The diffusive components are rejected through the demodulation process (Eq. 13).

$$I_{dc} = 1/3(I_1 + I_2 + I_3) \tag{12}$$

$$I_{ac} = \sqrt{2}/3\,(\sqrt{(I_1 - I_2)^2 + (I_2 - I_3)^2 + (I_3 - I_1)^2}) \tag{13}$$

Thus, we obtain a depth controlled image, or AC image, which highlights only the reflected photons that experience fewer scattering events: those from the superficial layer of the sample. The conventional diffuse reflectance image or DC image can also be recovered from I_1, I_2 and I_3 using Eq. 12.

4.2.3 pSFDI Imaging System

We developed a pSFDI imaging system, as shown in Fig. 4.2, to perform fiber orientation mapping on native tissues. Compared to a standard SFDI imaging system, pSFDI has a rotating linear polarizer that serves as both the polarizer for illumination and analyzer for imaging. Sinusoidal patterns with a phase shift of 0^o, 120^o and 240^o at a spatial frequency $f=1mm^{-1}$ were generated by a digital micromirror device (DMD) (Lightcrafter, Texas Instruments) and projected onto the sample under 490nm LED illumination. The projection unit was custom modified to achieve low magnification projection, which increased the achievable spatial frequency. A linear polarizer was mounted on a motorized rotational stage and was rotated over a 180-degree range with a step size of 5 degrees. At each polarization angle, a high-resolution camera (piA2400-17 gm/gc, Basler) recorded the three phase-shifted reflectance images. The camera has a native resolution of 2456x2058 pixels and has a pixel size of 3.45 microns. A Schneider 70mm lens (TELE-XENAR 2.2/70) with an F/# of 2.2 was used. The imaging field was approximately 22mm x 14mm. Automated custom software written in LabVIEW controlled the system, and required approximately 90 seconds for full image acquisition. The DMD system was operated in 'stored-pattern-sequence' mode to avoid internal gamma correction.

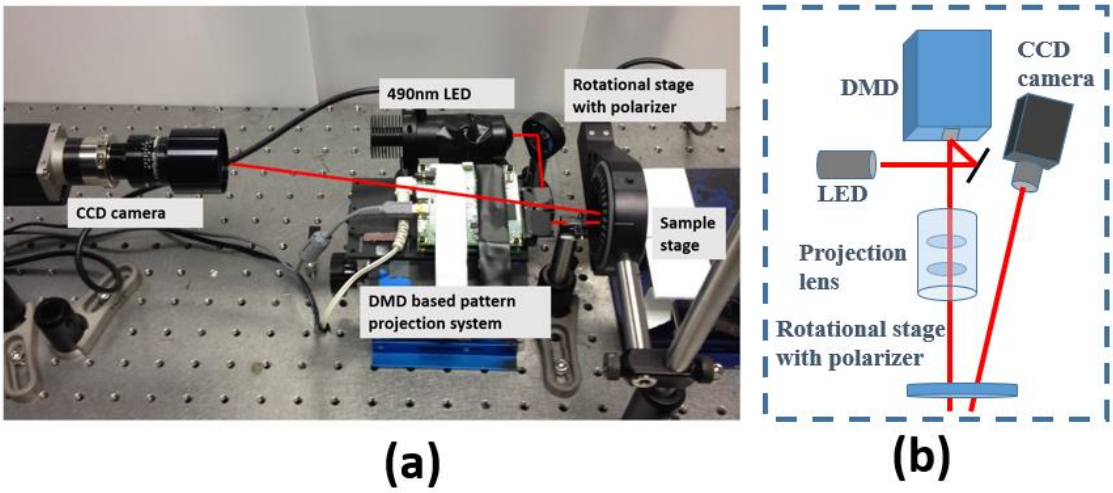

Figure 4.2 (a) Color picture of pSFDI imaging system. (b) Schematic of the pSFDI imaging system

4.2.4. ex-vivo Tissue Imaging

Based on the simulation results, we performed *ex-vivo* tissue imaging to demonstrate the technique. Both fresh bovine tendon and porcine aortic valve leaflet tissue (PVL) were imaged. Bovine tendon was chosen for a reference material as the collagen fibers typically run longitudinally along the length of the tendon. In addition, the gross fiber direction is observable by eye, which allows for quick validation checks. High degree of fiber orientation has been previously studies(74). Cardiac valve leaflet tissues, especially aortic and aortic cusps, have been well studied (60, 75, 76). These leaflets typically display characteristic fiber orientations, with fibers running along the circumferential direction. For that reason, and because leaflet tissue exhibits regional variation in fiber alignment, aortic valve leaflet tissue was studied to demonstrate the capability in sample-wide fiber orientation quantification with the pSFDI system.

4.2.4.1 Second-harmonic generation (SHG) imaging

Before fiber orientation mapping, we performed two-photon imaging to determine collagen fiber diameters in PVL. This diameter information was used in the simulation to improve the accuracy of the model, as well as to help form a preliminary understanding of PVL microstructure. Aortic valves were dissected from fresh porcine hearts and were stored temporarily in phosphate-buffered saline (PBS) prior to imaging. The SHG images of the collagen fiber networks in PVLs were obtained with a commercial two-photon microscope (Ultima System, PRAIRIE Technologies) at 900nm. The PVL was placed on a glass slide and covered by a cover slip during imaging. A 20x water immersion objective was used.

4.2.4.2 pSFDI imaging and sample preparation

We mapped the fiber orientation of *ex-vivo* bovine tendon, *ex-vivo* two-layer bovine tendon, PVL and combined tendon-PVL samples using pSFDI. The fibrosa side of the PVL was imaged. The fibrosa layer has high collagen concentration and dense fiber organization. Bovine tendon sections were sectioned from intact full tendons. The sections were cut parallel to the longitudinal direction of the tendon such that the collagen fiber direction was in-plane. To image with pSFDI, samples were placed flat against 2x3 inch glass slides and placed in the imaging field to reduce the specular reflection from the sample. The combined PVL-bovine tendon samples required the placement of a bovine tendon section immediately against the PVL and clamping the two to a glass side with non-destructive silicone rubber. The PVL-bovine tendon sample was larger than the projected illumination

area; thus the sample was imaged twice and stitching was performed in post processing to form a whole image.

4.2.4.3 Small angle light scattering (SALS) imaging and sample preparation

The same PVL samples used in pSFDI were then imaged with SALS (after fixation and clearing) as an accuracy check and comparison. The SALS imaging technique has been previously described in detail and validated (34). Briefly, the scattered light of a 5mW HeNe laser (λ=632.8nm) was examined to determine the local fiber orientation. By raster scanning a sample through the beam path a sample-wide fiber orientation map was acquired. The porcine aortic valve leaflets were prepared for SALS imaging. Submersing the leaflets in 4 increasing grades of PBS/glycerol solution ranging from 50 to 100 percent glycerol cleared the tissue by extracting diffusive water without altering sample geometry. Cleared PVL samples were placed, without compression, between two glass slides and raster-scanned by a SALS device, with total scanning time of 30 minutes.

4.3. RESULTS

4.3.1 Cylinder Scattering Simulation

Fig. 4.3 shows the collagen fiber network from a localized region of the leaflet tissue. The size of the collagen fibers is relatively consistent with small variation. Fiber diameters were distributed approximately between 1 μm to 3 μm. The measured range of fiber diameter information was used in the model described in Section 2. Fig. 4.4a shows a plot of the simulated back-scattered light from cylinders versus the incident polarization over a 180-

degree polarization range. The simulation results show two peaks over 180 degrees. The higher peak is located at 30 degrees, which corresponds to true local fiber orientation, and the lower peak is 90 degrees away from the higher peak. Thus, the local fiber orientation can be determined by tracking the location of the higher peak.

Collagen fibers consist of hundreds of collagen fibrils with diameters ranging from 260nm to 410nm(77). We also simulated the scattering property of collagen fibrils and the result is shown in Fig. 4.4b. Comparison between Fig. 4.4a and Fig. 4.4b suggested that both collagen fibers and fibrils had similar scattering property.

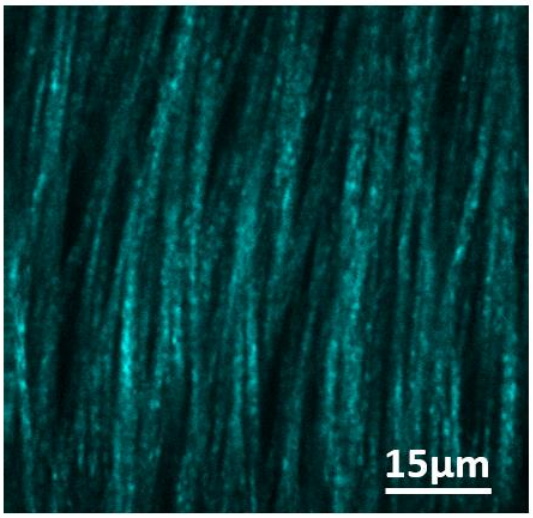

Figure 4.3 SHG image shows the collagen fibers in porcine aortic valve leaflet tissue

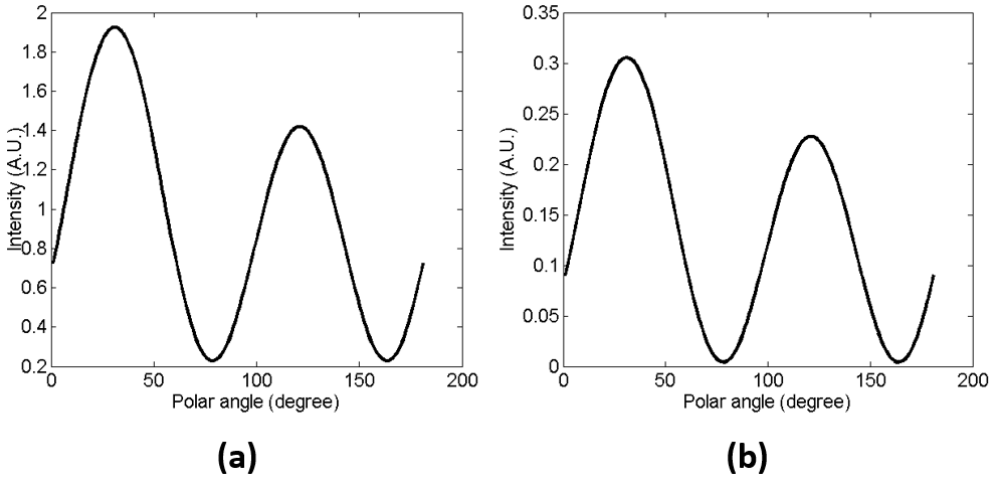

Figure 4.4 Polarization dependent back-scattered light over 180-degree polarization range for (a) collagen fibers and (b) collagen fibrils. Two peaks can be identified. The higher peak indicates that illumination polarization is parallel to the fiber orientation, while lower peak indicates they are perpendicular

The fiber orientation distribution simulation result shown in Fig. 4.5 suggests that two distinct peaks still can be identified over 180 degree range even with fiber orientation distribution. Higher peaks are located at 30 degrees, which also corresponds to preferred local fiber orientation. However, as the fibers become more spread out, both the higher peak intensity and lower peak intensity decrease. This trend correlates with the alignment quality of fibers. For totally randomly oriented fibers, the scattering profile is flat over 180 degree range.

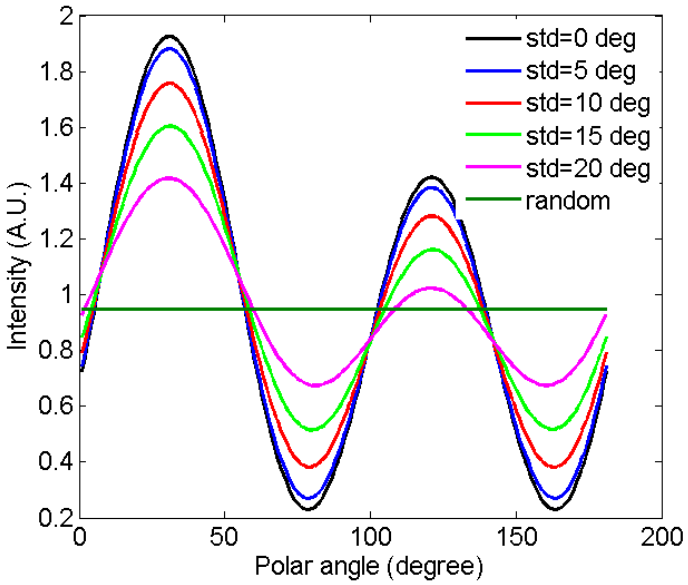

Figure 4.5 Polarization dependent back-scattered light over 180-degree polarization range for 6 fiber distributions. The higher peaks locate at 30 degree for normal distribution. With higher fiber orientation deviation, both higher peak and lower peak intensity decrease. No peak can be found for random distribution

4.3.2 Collagen Fiber Orientation Mapping on Bovine Tendon

Fig. 4.6 shows the fiber orientation map of two bovine tendon samples quantified using the pSFDI imaging system. The red dashed rectangle in the standard color image shows the imaged area. The blue arrow indicates the gross fiber orientation for each bovine tendon based on visible features. The mean fiber orientation for the left and right sections of bovine tendon are about -80 degrees and 60 degrees, respectively. Fig. 4.6(b) shows the back-scattered intensity from both DC and AC components over a 180-degree range from one pixel indicated by the black square in Fig. 4.6(a). Note that the data in the plot were from an individual pixel and no averaging was used. The black square was only for indicative purpose to highlight the location of data. The incident polarization modulated the reflectance intensity. Two peaks can be identified, which agrees with the simulation. The

location of the higher peak indicates the local fiber orientation. The polar plots for both DC and AC show a very similar shape, although the DC plot has slightly higher SNR than the AC one. In terms of relative intensity, the AC component is only about 47% of the DC peak intensity, which confirms diffuse background rejection.

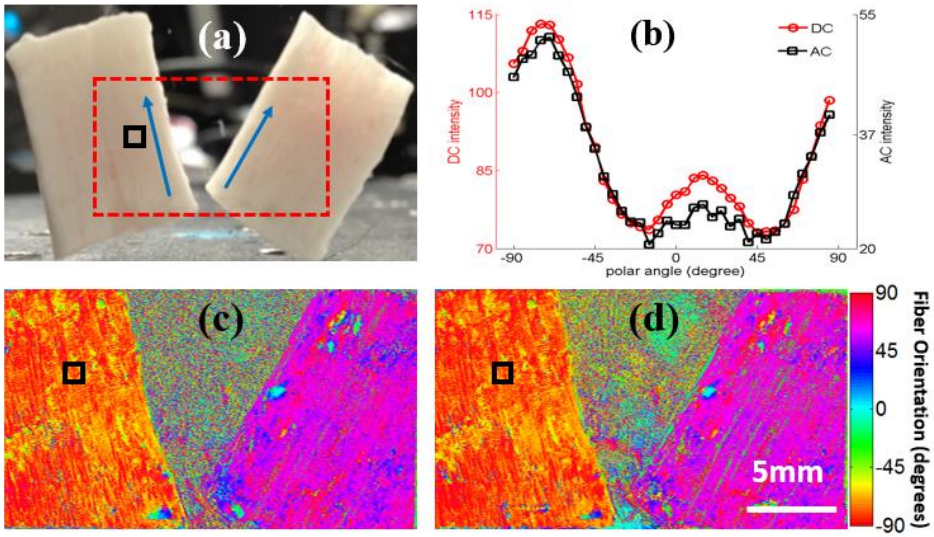

Figure 4.6 Collagen fiber orientation mapping on bovine tendons. (a) Blue arrows indicate the gross fiber orientation of the bovine tendons. Red rectangle shows the imaged area. (b) Back-scattered intensity plot over a small region indicated by a black square using both DC and AC components. (c) Fiber orientation map extracted using on AC components. (d) Fiber orientation map extracted using DC component

Fig. 4.6c and 4.6d show the fiber orientation map retrieved based on DC and AC components, respectively. These images were generated by identifying the angle at which the peak intensity was observed across polarization angles. The color represents preferred local fiber orientation. Overall, the two maps appear very similar, and the color-coded orientation map agrees well with the expected fiber orientation based on visual inspection. The bovine tendon has very consistent fiber orientation through its depth. Thus, using both DC and AC components, the fiber orientation map can be accurately quantified over a large

area of the sample. This experiment demonstrated that pSFDI imaging was able to accurately retrieve the fiber orientation on a sample with simple structures and non-varying layers. For such samples, both DC and AC based orientation maps showed similar results.

To further explore the depth-controlled imaging capability of pSFDI, we imaged a two-layer model with two thin slices of fresh bovine tendon. The layers were arranged such that their preferred fiber orientations cross-aligned at ~ 45 degrees with top and bottom layer thicknesses of approximately 200μm and 1mm respectively. Collagen fiber orientation maps were retrieved using pSFDI at two spatial frequencies: 0.5 and 0.09mm^{-1}.

Orientation maps gathered from a two-layer bovine tendon sample depicted the capability of the pSFDI system to discriminate top layer fiber information. The bottom tendon layer was visible underneath the top layer (Fig. 4.7(a)). When the sample was imaged solely with PLI with no spatial pattern, it is clear from the yellow coded areas in the top layer region that collagen orientation was falsely retrieved (Fig. 4.7(b)), as bovine tendon should display a highly uniform orientation. Without depth control, the acquired signal represents photons that fully penetrated the top layer and interacted with the lower layer.

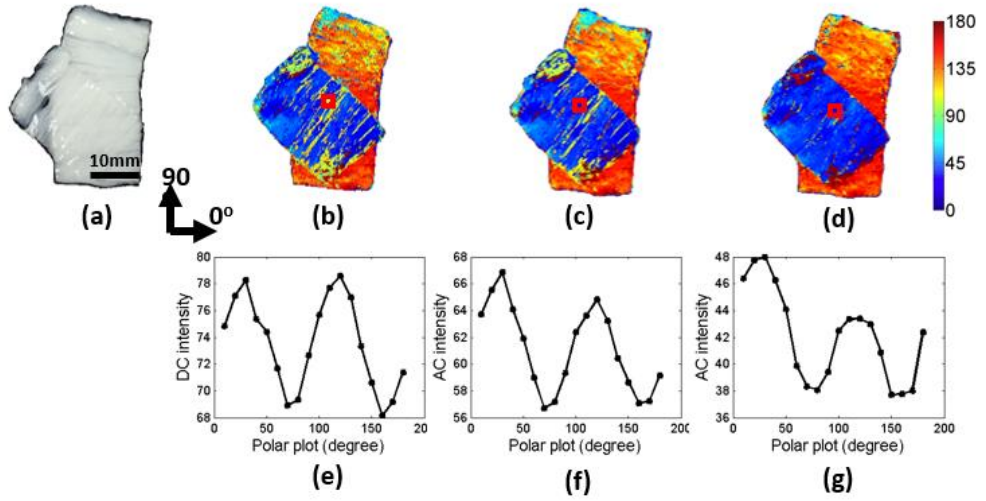

Figure 4.7 Depth controlled pSFDI imaging of a two-layer bovine tendon sample (a). The collagen fiber orientation map retrieved using polarized light imaging without spatial pattern in map (b). The collagen fiber orientation maps (c) and (d) retrieved at spatial frequencies 0.09 and 0.5 mm-1, respectively. The intensity plot (e-g) for localized regions in (b-d), respectively

By introducing structured illumination and by tuning the spatial frequency from 0.09 mm^{-1} to 0.5 mm^{-1} (Fig. 4.7(c-d)), top layer discrimination was achieved. The effective penetration depth decreased from over 1000 μm to approximately 300 μm estimated according to Eq. 11. Thus we noticed that retrieved collagen fiber orientation became more consistent over the top layer region, which was because the light primarily interacted with the top layer, and the contribution from the underlying layer was effectively eliminated. The polar plots (Fig. 4.7(e-g)) from the region indicated by red square demonstrated the higher peak location moved from ~120 degree to ~40 degree as the spatial frequency increased.

4.3.3 Collagen Fiber Orientation Mapping on Heart Valve Leaflet

We performed two experiments on *ex-vivo* porcine PVL tissues to further examine the pSFDI performance on samples with complex structures. The leaflet was imaged alone first. The red rectangle in the standard color image illustrates the imaged area in Fig. 4.8a-1. Fig. 4.8b and 4.8c show fiber orientation maps extracted using both DC and AC components, respectively. Overall, the two orientation maps show very similar results, and they have a good agreement with the fiber orientation map generated using SALS imaging shown in Fig. 4.8d. By examining polarization dependent scattering (Fig. 4.8e) over a 180-degee polarization range for both DC and AC components in small regions indicated by the black squares in Fig. 4.8b and 4.8c, we noted that the polar plots agreed well with each other and also with the simulation results. The DC component has higher overall intensity than AC component. This is because the diffuse photons were rejected in demodulation process. Two peaks can be identified in both plots, and the higher peak positions match with each other. However, Fig. 4.8b suggests that there are a few small regions where retrieved fiber orientation may not be reliable compared with the AC component based results, as indicated by black arrows. Similar features can also be identified in the SALS based orientation map shown in Fig. 4.8d. This observation indicates that the fiber organization may be complex in those regions as confirmed by previous study (75). In that study, fiber orientation of fibrosa and ventricularis layer were studied individually by separating these two layers from an intact leaflet. In most regions of a leaflet especially in the center region, the fiber orientation are comparable for fibrosa layer and ventricularis layer. However, towards the edge of the leaflet, the fibrosa and ventricularis layers display different fiber orientations. Transmission based imaging or conventional reflection based imaging is not

able to well separate there two layers, thus, only through-the-thickness results can be obtained. By introducing the SFDI imaging, the signal from the superficial layer/fibrosa layer can be enhanced. The AC based orientation map shows the orientation transition is much smoother in those regions. This study indicates that both AC and DC based methods can quantify fiber orientation in the center region of the leaflet where fiber orientation is less depth dependent. However, towards the edge of the leaflet, the fibrosa and ventricularis layers show different fiber orientations. Thus AC component based method is able to quantify fiber orientation in superficial layer without being affected by deeper tissue by using optical sectioning.

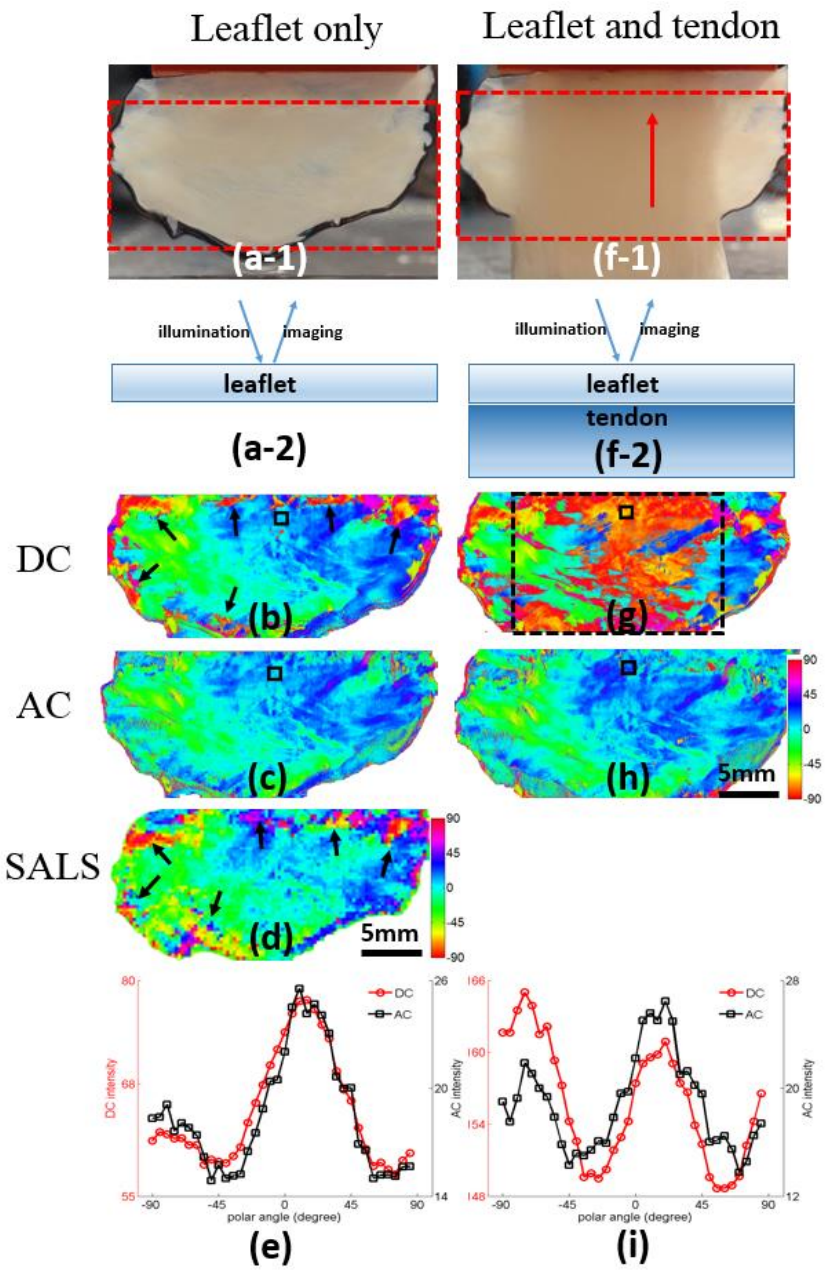

Figure 4.8 pSFDI imaing on PVL (a-1 and 2) and PLV-tendon combination (f-1 and 2). DC component based fiber orientaion maps (b and g) for PLV and PLV-tendon combination, respectively. AC component based fiber orientation maps (c and h) for PLV and PLV-tendon combination, respectively. A SALS based orientation map (d) for PLV was obtained for comparison purpose. Polar plots of both AC and DC components from a small region indicated by black sqares (b and g) for both PLV (e) and PLV-tendon combination (i) respectively. Black arrows in (b) and (d) indicate unreliable fiber orientation. Dashed black rectangle in (g) indicates the overlapping region of PLV-tendon combination

To demonstrate that fiber orientation can be better quantified by rejecting diffuse photons from deeper tissue using the AC component, we placed the same leaflet on a thinly sliced bovine tendon with ~1mm thickness shown in Fig. 4.8f-1 and Fig. 4.8f-2, and mapped the fiber orientation using both DC and AC components. The red arrow in Fig. 4.8f indicates gross fiber orientation of the tendon. Fig. 4.8g and h show that there is a significant difference between retrieved fiber orientation maps. In the DC component based map, half of the orientation map shows the fiber orientation of bovine tendon in the overlapping region. On the other hand, using the AC component, the fiber orientation of the leaflet still can be quantified even with the presence of the highly scattering bovine tendon layer. This can be qualitatively understood as follows. In the region where the leaflet is thin, the back-scattered light intensity from the leaflet is small compared with the one from the bovine tendon layer. Thus, the detected signal carries orientation information mainly from the bottom layer. Once SFDI is introduced, it eliminates the highly diffuse photons from this bottom bovine tendon layer, and highlights the back-scattered photons from the top layer, which allows for the fiber orientation retrieval on superficial layer of the leaflet. This phenomenon can be further confirmed by plotting the intensity variation over 180-degree polarization range over a small region indicated by the small black square in Fig. 4.8g and h. Fig. 4.8i indicates 1) AC component has much lower intensity due to diffuse photon removal. Only about 17% of the peak intensity is detected in AC component compared with DC component. 2) The higher peak locations are different for both AC and DC components, which indicates the bovine tendon structures mainly determine fiber orientation without diffuse background rejection. The diffuse photons were successfully

suppressed by using demodulation at high spatial frequency, which resulted in improved fiber orientation retrieval accuracy.

4.4 DISCUSSION

In this paper, we described a new imaging technique, pSFDI, for mapping the fiber orientation of native tissues by utilizing polarization dependent scattering. We significantly improved the quantification accuracy in multilayered samples by rejecting the diffuse photons to limit the sampling depth using SFDI imaging technique. Compared with Konecky's approach, pSFDI technique is different in the following ways: 1) pSFDI probes the fiber orientation by rotating the polarization of the illumination instead of rotating the illumination patterns. 2) The spatial patterns in pSFDI are used to reject diffuse background and to control the imaging depth instead of directly probing the fiber orientation. In conventional polarization difference imaging, the photons from superficial layer can be extracted by taking the difference between parallel detection and perpendicular detection(5). The parallel detection captures photons with its original polarization state from both superficial and deeper tissue. The perpendicular detection removes the specular reflection and photons from superficial layer; thus the signal from deeper tissue can be highlighted as suggested by Morgan *et al*(78), which is the main difference compared with superficial detection in pSFDI. The polarization difference imaging is able to perform superficial detection, however, the imaging depth solely depends on the depolarization capability of the sample. In pSFDI imaging, parallel detection is used to collect photons with its original polarization state from superficial layer to deeper tissue. After the

introduction of structured illumination, the imaging depth then depends on both sample's optical property and spatial frequency of the pattern. By changing the spatial frequency, the imaging depth can be controlled. Thus, the superficial detection is possible.

The experimental data was processed using both DC and AC components. It is apparent that, for samples with simple structures like bovine tendon, DC and AC based results did not show much difference. This suggests that, for such samples, structured illumination does not add extra benefit. Thus, planar illumination may suffice and the imaging time can be reduced by 66%. However, for the naturally multilayered tissues, like heart valve leaflets, and more extreme artificial samples like the leaflet-tendon combination, AC component based results justified the structured illumination for improved superficial layer quantification accuracy. At a spatial frequency of $1mm^{-1}$, the penetration depth is estimated as 159 μm using Eq. 11, which is thinner than the average thickness of 265 μm for a typical leaflet (60). Thus, imaging at this spatial frequency, only the superficial layer of the leaflet is sampled, and we can obtain the layer specific fiber orientation map.

In our study, we used collagen fibers instead of collagen fibrils to model the light scattering property. A collagen fiber consists of hundreds of densely packed collagen fibrils. It is likely that these fibrils form a composite refractive index inside the fiber; thus, scattering is from the refractive index mismatch between extracellular matrix and densely packed fibrils. Since fibers consist individual fibers, part of scattering could be from fibrils. Our simulation on individual fibrils with diameter between 260nm to 410nm (77) suggested that fibrils have similar scattering property compared with fibers shown in Fig. 4.4. However, given the nature that fibrils are densely packed, we think individual fibers are

major scatterers, which is consistent with previously reported light scattering studies (39, 59, 63).

We used a collection of fibers with multiple diameters to study the scattering property from the bulk tissue. As a first order approximation, only a mono-layer of fibers was modeled. In this model, one photon primarily interacts with one fiber. Thus, we were able to study the light-tissue interaction using an analytical method. However, this simplified model does not reveal full light-tissue interaction in bulk tissue. This model is sufficient to represent the fiber scattering property, and experimental results agree well with simulation results. The light-tissue interaction is more complex in real bulk tissues. The photons are mainly forward scattered and will interact with multiple layers of fibers rather than a single fiber layer. Furthermore, only cylindrical scatterers were considered in the model, while in real tissue, a much more complex array of both spherical and cylindrical scatterers exist. A Monte-Carlo model accounting for both spherical and cylindrical scatterers would be beneficial to fully study bulk tissue scattering.

Compared with other polarization based methods, pSDFI imaging requires only one linear polarizer versus at least 2 polarizers for other methods. This simple configuration significantly reduced the system calibration requirement. Furthermore, this configuration allowed for direct visualization of the light-structure interaction via the polar plot. One can estimate the local fiber orientation by locating the higher peak on the polar plot.

We quantified the fiber orientation directly from the polar plot of the back-scattered intensity by tracking the location of the main reflectance peak. Although straightforward,

the accuracy is limited by the angular step size during the imaging. In our study, a five degree step size was used. To increase the accuracy, a smaller step size can be used at the expense of longer imaging time. Potentially, the fiber orientation can also be quantified by fitting the experimental data to analytical model, which may tolerate a larger angular step-size. Such fitting-based method may be less time efficient, but it may have the potential to extract richer information other than orientation. Furthermore, we noted that some tissues might have very complex fiber organization in certain regions, where two distinct peaks could be reduced to one large peak. Fitting-based method may fail in these regions. However, the preferred fiber orientation may still be determined by just tracking the peak position.

With our current pSFDI implementation, we were required to collect two separate images and stitch them together to accommodate the full leaflet. This is not a limitation of pSFDI imaging, but of our specific hardware. The 0.3'' DMD chipset used here is relatively small and has lower resolution compared to 0.55'' and 0.7'' chipsets. In pSFDI imaging, the spatial patterns are represented by micromirrors. Fewer micromirrors per period are, higher the spatial frequency will be. Also, the spatial frequency can be increased by reducing the projection magnification. To achieve a spatial frequency of f=1mm^{-1}, we used 18 micromirrors to represent one spatial period and we also reduced the projection magnification. As a result, the projection field was relatively small, thus the leaflet was imaged twice to get the whole coverage. With a bigger chipset, the projection area will be bigger and the entire leaflet could potentially be imaged at high spatial frequency without the need for image stitching.

4.5 CONCLUSION

In this chapter we described a novel imaging modality, pSFDI, which combines polarized light imaging and spatial frequency domain imaging techniques to perform fiber orientation mapping on superficial layer by rejecting diffuse photons and controlling the imaging depth at high spatial frequency. In the case of samples having simple fibrous structures, pSFDI imaging may be reduced to the polarized light imaging for increased acquisition speed while preserving accuracy. The small form factor and fast imaging speed allow for integration with mechanical testing devices to study sample response under controlled deformation. pSFDI imaging promises to be a versatile tool in matters concerning fibrous tissue microstructure.

CHAPTER 5 : HANDHELD SFDI IMAGING PLATFORM FOR SKIN IMAGING

5.1 INTRODUCTION

Quantifying the skin properties has the potential towards better understanding of skin diseases and may lead to more accurate clinical diagnosis. Many techniques have been reported to quantify the skin properties, such absorption and scattering properties, biochemical compositions and oxygen saturation. Based on these properties, structural and physiological changes in skin can be studies. The techniques used to study skin typically fall into two categories: point measurement based method (43, 79-81) and image based method(82). For point measurement, a skin lesion may need to be measured multiple times to obtain good representation of the lesion. Skin diseases typically are spatially heterogeneous. Even with multi-spot measurements, skin features may not be sampled adequately. Thus, image based quantitative skin characterization is more desirable, especially when lesion margin detection is needed. However, wide-field skin property characterization was challenging until the development of spatial frequency domain imaging (SFDI). With SFDI, skin properties such as absorption and scattering properties, can be non-invasively assessed. When it is coupled with hyperspectral imaging and fluorescence imaging, even richer skin properties, such biochromophore concentration mapping and absorption reduced fluorescence, can be quantified. Saager *et al* and Daniel *et al* demonstrated that by quantitatively evaluate the skin optical properties, a better dosimetry strategy can be formed and applied to non-melanoma skin cancer treatment (24,

83). Mazhar et al studies the biochemical composition change of port wine stain in response to laser therapy(84).

Although several skin studies has been done using SFDI imaging, clinical skin imaging still face challenges. Skin conditions can virtually be found anywhere on the body. There are many hard-to-reach regions, such as head and neck. A typical SFDI imaging system is generally large in size. Even if an imaging system adopted articulating mounting strategy, it is difficult to image these regions. Furthermore, compared to conventional reflectance imaging, SFDI imaging takes 3 time longer imaging time, which makes SFDI imaging more susceptible to motion artifacts, especially, when hyperspectral imaging and fluorescence imaging are incorporated.

To address these issues, we developed a handheld SFDI imaging system to perform both hyperspectral imaging and fluorescence imaging in a clinical setting. We performed comprehensive characterization to reveal multifaceted properties of skin diseases including optical, biochemical and fluorescence properties as well as structure emphasized image.

5.2 METHODS AND MATERIALS

5.2.1 Imaging System Development

We developed a handheld SFDI imaging platform shown in Fig. 5.1 for clinical skin imaging. We separated the light source (Fig. 5.1(a)) from the imaging head (Fig. 5.2 (b)) to make the handheld device compact and flexible. The light was delivered via a liquid

light guide (Part # 77568, Newport). We integrated both hyperspectral imaging and fluorescence imaging in handheld device to expand its imaging capability.

A digital light projection evaluation module (Lightcrafter, Texas Instruments) was used to generate and project the patterns. The light engine of the module was custom modified and the projection unit was freed from the light engine, which allowed for shorter and adjustable projection distance. Of particular importance, we inserted a piece of thin circular glass at the front end of the imaging head shown in Fig. 5.1(d and e), which served two purposes: 1) reduce the skin contour effects by gently pressing the skin; 2) reduce the specular reflection by applying gel between glass and the skin. The glass windows has the raised edge around it to increase the friction between the skin and the imaging head which reduces the relative motion. The raised edge also prevents the skin from being hardly pushed by the glass window. A CCD camera (AVT Stingray 145B) with a 25mm lens was used to acquire images. The optical axis of the camera was tilted about 5 degree from the projection axis to avoid specular reflection from the imaging window.

In the light engine, we used an LED assembly with 6 individual LEDs shown in Fig. 5.1(c) (Part # SP-02, Luxeon Star LEDs), which operated at 470, 505, 530, 590, 617 and 655nm. A 395nm UV LED (M395L3, Thorlabs) was used for the fluorescence imaging. Excitation light was filtered with a 400nm lowpass filter (T400lp, Chroma) before it was coupled into the light guide. Fluorescence was collected with a bandpass filter centered at 550nm (Part #: 84-784, EdmundOptics), which can be toggled between fluorescence imaging and reflectance imaging using a flip mount (MFF101, Thorlabs).

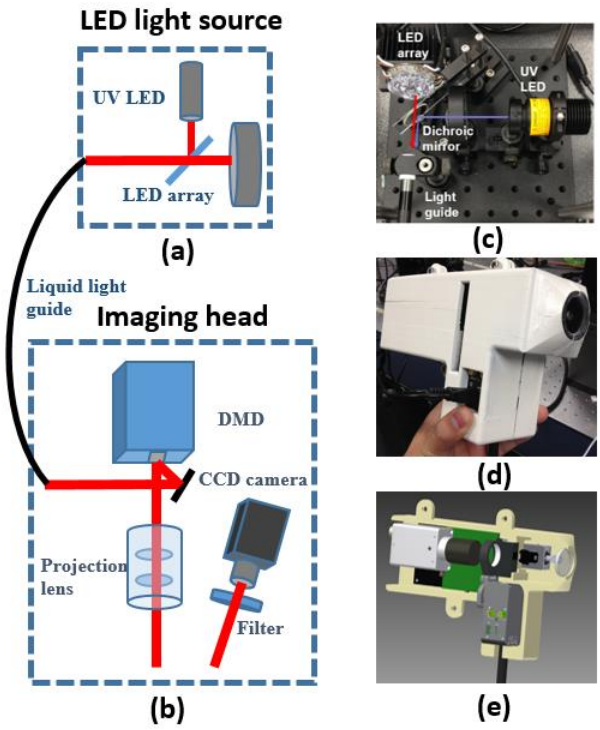

Figure 5.1 System schematic for LED light source (a) and Imaging head (b), (c) Color picture of LED light source configuration (c), (d) color picture of imaging head, (e) 3D rendering of imaging head

We wrote a custom controlling software in LabVIEW so that both reflectance imaging and florescence imaging acquisition were automated. Of particular importance, the DMD was operated in ‘stored sequence mode’ to avoid internal gamma correction. The system was placed on a push cart to further improve its mobility. Figure 5.2 shows the clinical imaging system.

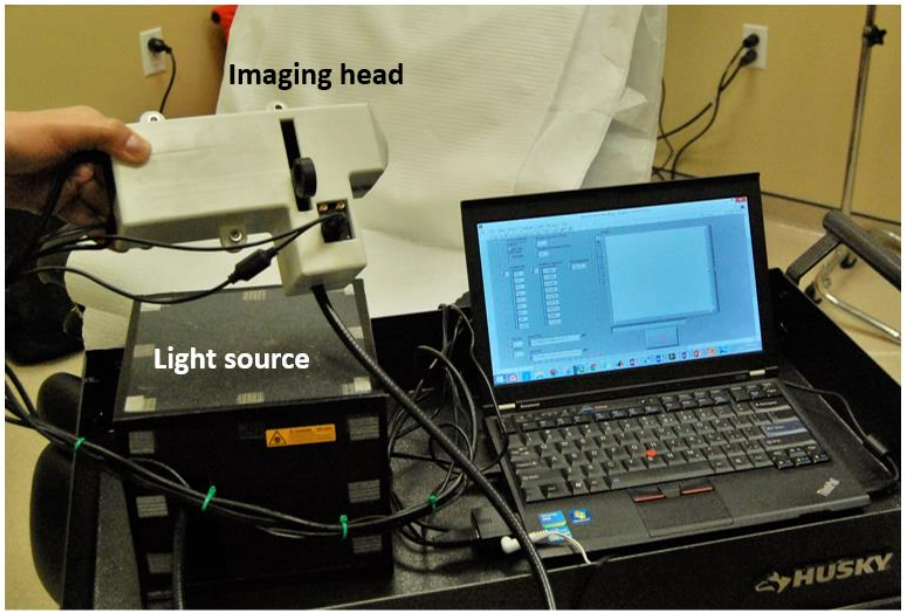

Figure 5.2 Clinical imaging system in a clinical setting

5.2.2 Clinical Skin Imaging

With the imaging system, we conducted clinical skin imaging at Dell Medical School. This clinical study was approved by institutional review board (IRB) at both the University of Texas at Austin and Seton Healthcare. A total of 48 lesions from 31 patients, both benign and malignant, were imaged. The patients participated the study voluntarily after providing informed consent. During the imaging, surgical lubricant was applied to patient's skin, which served as refractive index matching material and reduced specular reflection from the skin. Both hyperspectral reflectance imaging at six wavelengths and fluorescence imaging were conducted at two spatial frequencies of $f=0.2mm^{-1}$ and $f=0.6mm^{-1}$. The total imaging time ranged from about 30 seconds to 45 seconds depending on lesion types. A regular color picture of the lesion were taken after clinical imaging.

5.2.3 Image Processing Methods

In this section we will discuss imaging processing methods that we used to analyze and visualize skin properties: color SFD image, optical properties, biochromophore concentration mapping, and absorption reduced fluorescence. We used AC component at high spatial frequency for color SFD imaging and absorption reduced fluoresce imaging. Furthermore, we mapped total hemoglobin and melanin concentration distribution based on absorption coefficients at 6 wavelengths.

In SFDI imaging, three two-dimensional spatial patterns with phase shifts of 0, 120 and 240 degrees are projected onto tissue surface, and corresponding reflectance intensity images, I_1, I_3 and I_3, are acquired. DC and AC images, I_{DC} and I_{AC}, are obtained through a demodulation process shown in Eq.12 and 13 (16). Both AC and DC images are functions of spatial frequency f and wavelength λ. DC image is same as if the sample is imaged using planar illumination. AC image is also known as SFD intensity image and it is dependent on spatial frequency. Higher the spatial frequency is, shallower the imaging depth will be (16). By tuning the spatial frequency and wavelength, tissue properties can be selectively examined. In visible range, tissue absorption and scattering decrease as illumination wavelength increases. As the spatial frequency increases, AC image is less sensitive to absorption as the sampling depth decreases and more sensitive to scattering property.

$$I_{DC}(f,\lambda) = 1/3(I_1(f,\lambda) + I_2(f,\lambda) + I_3(f,\lambda)) \quad (12)$$

$$I_{AC}(f,\lambda) = \sqrt{2}/3\left[\sqrt{(I_1(f,\lambda) - I_2(f,\lambda))^2 + (I_2(f,\lambda) - I_3(f,\lambda))^2 + (I_3(f,\lambda) - I_1(f,\lambda))^2}\right] \quad (13)$$

5.2.3.1 Depth controlled imaging

In conventional reflectance imaging, the imaging depth is highly dependent on wavelengths. The effective penetration depth is determined by the tissue absorption and scattering properties, and can be described as $\delta_{eff}^{'} = (\sqrt{3\mu_a(\mu_a + \mu_s^{'})})^{-1}$, where μ_a and $\mu_s^{'}$ are absorption coefficient and reduced scattering coefficient. As the wavelength increases, both μ_a and $\mu_s^{'}$ decrease for typical biological tissues. Thus, generally imaging at higher wavelength permits greater imaging depth. With the structured illumination, the imaging depth can be further tuned by varying the spatial frequency at given wavelength. For a scattering dominant medium, the spatial frequency dependent imaging depth can be analytically described as $\delta_{eff}^{'} = (\sqrt{3\mu_a(\mu_a + \mu_s^{'}) + (2\pi f)^2})^{-1}$, where f is the spatial frequency. As the spatial frequency increases, the effective penetration depth decreases. One thing needs to be noticed is the sample's optical properties sets the deepest imaging depth. With structured illumination, the imaging depth can only be tuned towards shallower depth. Although analytical solution is only available for scattering dominant medium, the role of spatial frequency dependent effect can be qualitatively applied to more general medium.

One unique property of SFDI imaging is, at high spatial frequency, modulated reflectance is more sensitive to sample's scattering property and less sensitive to absorption property, which allows for skin imaging from a new perspective. In clinical imaging, we used two spatial frequency 0.2mm^{-1} and 0.6mm^{-1} for both reflectance and fluorescence imaging. Thus the depth controlled reflectance image can be obtained by simply extracting the AC component at corresponding spatial frequency.

5.2.3.2 Color rendered reflectance imaging

A typical color image is composed of red (r), green (g) and blue (b) channels. Likewise, to render a color SFD image, we imaged the sample using three wavelengths of 470, 530 and 655nm to represent r, g and b channels, respectively. Two spatial frequencies, f=0.2mm^{-1} and f=0.6mm^{-1}, were used to investigate spatial frequency dependent skin visualization. Both AC and DC intensity images were normalized to a 99% reflectance standard (Labsphere) to obtain corresponding reflectance images as shown in Eq. 20 and 21 before color rendering.

$$R_{DC} = 0.99 * (I_{DC} / I_{std}) \tag{20}$$

$$R_{AC} = 0.99 * (I_{AC} / I_{std}) \tag{21}$$

Thus color reflectance image can be represented using reflectance images R_r, R_g and R_b as

$$R_{color} = (\alpha R_r, \beta R_g, \gamma R_b) \tag{22}$$

where R_{color} is the color SFD image; α, β, and γ are relative contribution of r, g and b channels, respectively. Both DC and AC reflectance images at two spatial frequencies were used to render color SFD image.

5.2.3.3 Absorption reduced fluorescence imaging

In fluorescence imaging, the fluorescence were collected using structured excitation with spatial frequencies of f=0.6mm^{-1}. The raw fluorescence images were demodulated and AC components were extracted using Eq. 13. The absorption in demodulated images were greatly reduced due to reduced imaging depth (85).

5.2.3.4 Optical properties and bio-chromophore mapping

The optical properties μ_a and μ_s' were retrieved at 6 six wavelengths using a GPULUT method as described in Chapter 2. Two quantities, modulation M and reflectance R, were calculated from the reflectance measurement (21), which were later used as searching index in LUT to extract μ_a and μ_s'.

$$R = \frac{I_{dc,sample} \times 0.99}{I_{dc,spectralon}} \tag{23}$$

$$M = \frac{I_{ac,sample} / I_{dc,sample}}{I_{ac,spectralon} / I_{dc,spectralon}} \tag{24}$$

To map the hemoglobin and melanin concentration distributions, we used a simplified skin model by assuming main chromophores are oxy-hemoglobin, deoxy-hemoglobin and melanin. Thus skin absorption can be modeled as a linear combination of the absorption from all chromophores shown in Eq. 25. The bio-chromophore concentration can be obtained simply by taking inverse of Eq. 25 as long as $n \geq m$. We used spectra of hemoglobin and melanin from Steve Jacques's compilation.

$$\begin{bmatrix} \mu_a(\lambda_1) \\ \vdots \\ \mu_a(\lambda_n) \end{bmatrix} = \begin{bmatrix} \varepsilon_1(\lambda_1) \cdots \varepsilon_1(\lambda_1) \\ \vdots \quad \ddots \quad \vdots \\ \varepsilon_1(\lambda_n) \cdots \varepsilon_1(\lambda_n) \end{bmatrix} * \begin{bmatrix} c_1 \\ \vdots \\ c_m \end{bmatrix} \tag{25}$$

5.3 RESULTS

The skin conditions we imaged in the clinic are highly divergent. In this paper, we selected three representative lesions shown in Fig. 5.3. to demonstrate the skin characterization capability of this handheld SFDI imaging system. The clinical diagnosis of the lesion

shown in Fig. 5.3(a). is granuloma annulare (GA). GA is ‘an immunologically mediated necrotizing inflammation that surrounds blood vessels, altering collagen and elastic tissue’. Although GA is local skin disorder, is it similar to many other serious conditions including subcutaneous nodules and annular lesions. The clinical color picture of GA looks pink with central depression. The second lesion, Fig. 5.3(b), was clinically diagnosed as basal cell carcinoma. The clinical diagnosis for the last lesion, Fig. 5.3(c), was seborrheic keratosis (SK). It is one of the most common of the benign epithelia tumors. However, some SK lesions may resemble melanoma and squamous cell carcinoma.

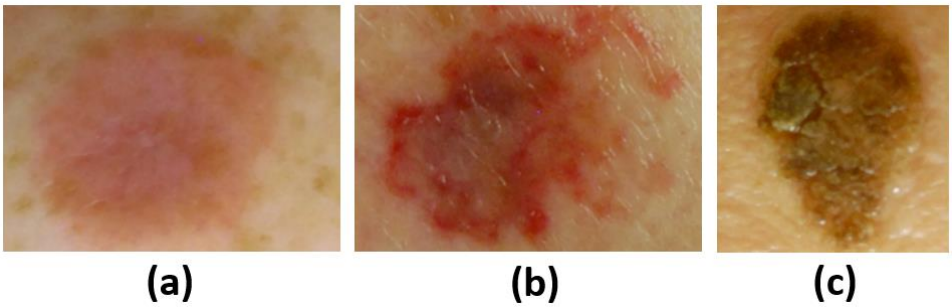

Figure 5.3 Color pictures of skin lesions (a) granuloma annulare (b) basal cell carcinoma (c) seborrheic keratosis

5.3.1 Color Reflectance Imaging

Fig 5.4(a) shows an irregular shaped lesion with high blood contents, which was clinically diagnosed as basal cell carcinoma (BCC). Within the lesion, color variation is also observed. Conventional hyperspectral images, Fig. 5.4(a-1, 4, 7), exhibit high absorption at 470nm and 530nm and low absorption at 655nm. By introducing structured illumination and increasing the spatial frequency from f=0.2mm^{-1} to f=0.6mm^{-1}, absorption at 470nm and 530nm is significantly reduced with only a few scattered absorbing spots can be

identified (Fig. 5.4(a-3 and 6)), which resulted in a reduced contrast between lesion and normal tissue. In Fig. 5.4(a-9), the lesion can barely be identified, which was partly because the absorption was very low at 655nm and partly because tissue structural changes was too small to alter tissue scattering property. By rendering color images for each individual spatial frequency, we obtained color SFD reflectance images shown in Fig. 5.4(a-10, 11, 12). Rendered color DC image, Fig. 5.4(a-10), compares very well with true color image shown in Fig. 5.4(a). At f=0.6mm^{-1}, the absorption from blood is reduced so greatly that the lesion looks almost transparent with only a few red absorbing spots. Other than that, the lesion looks similar to surrounding normal tissue, which may imply the scattering property are similar for both lesion and normal tissue. Comparing grayscale SFD reflectance images with color rendered SFD images, it is evident that skin lesion can be better comprehended and different skin features can be identified easily.

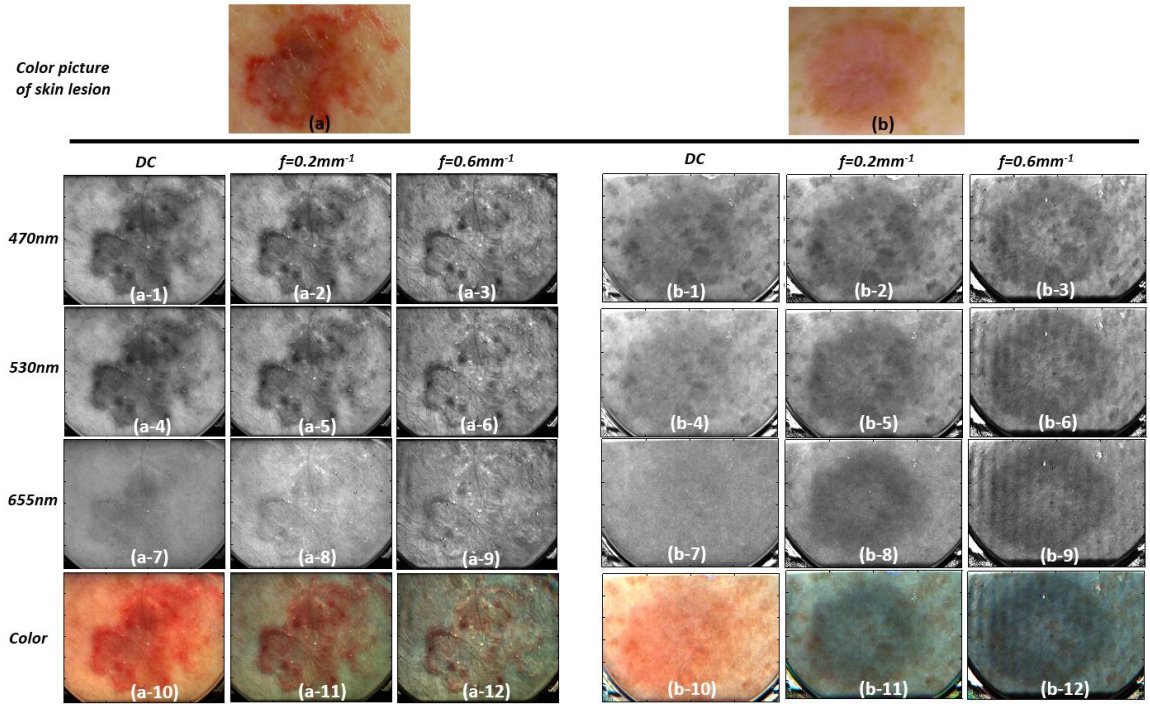

Figure 5.4 Color images of skin lesion: (a) basal cell carcinoma (BCC) and (b) granuloma annulare (GA); a(1-9) show SFD reflectance images at 470, 530, and 655nm for spatial frequencies of 0mm-1(DC), 0.2mm-1 and 0.6mm^{-1} for BCC; a(10-12) show color SFD reflectance images of BCC; b(1-9) show SFD reflectance images at 470, 530, and 655nm for spatial frequencies of 0mm-1(DC), 0.2mm^{-1} and 0.6mm^{-1} for GA; b(10-12) show color SFD reflectance

The lesion shown in Fig. 5.4(b) was clinically diagnosed as granuloma annulare (GA). GA is 'an immunologically mediated necrotizing inflammation that surrounds blood vessels, altering collagen and elastic tissue'(86), which means both absorption and scattering properties are changed in GA. At both f=0.2mm^{-1} and f=0.6mm^{-1}, SFD reflectance images showed an increased contrast for all wavelengths. Especially for f=0.6mm^{-1}, with reduced absorption effect, the contrast is manly from scattering property, which is evident by comparing Fig. 5.4(b-7) and Fig. 5.4(b-9). The enhanced contrast is from local scattering property change as a result of tissue structural alternation. The color SFD images (Fig. 5.4(b-10, 11 and 12)) revealed similar results to greyscale SFD images. Furthermore, in color images, we can identify that the contrast in DC images is mainly from increased

absorption, while at f=0.2mm^{-1} and f=0.6mm^{-1}, the contrast is mainly from reduced scattering. The source of contrast can't be easily identified in greyscale images because high absorption and low scattering result in dark appearance. One thing needs to be noted is the blue-shift effect towards higher spatial frequency in rendered color images. This can be qualitatively understood as: red light undergoes a longer transport pathlength, as a result, reflectance of red channel is more diffusive. The diffusive components are eliminated during the demodulation process, thus the absolute contribution from red channel is less at higher spatial frequency.

5.3.2 Optical Properties and Biochromophore Concentration Mapping

Optical properties of GA was extracted on 470, 505, 530, 590, 617 and 655nm. The optical property map is shown in Fig. 5.5. Both absorption coefficient and reduced scattering coefficient decrease as wavelength increases. In absorption map, both lesion and skin features, like freckles, show high absorption, especially at lower wavelength. In absorption map, the lesion can't be easily identified. This is because other skin features also showed similar absorption. In scattering map, it is clear that skin lesion is far less scattering than its surround normal tissues. The center portion of the lesion is slightly more scattering than

the rest part of the lesion. In addition, the lesion shape can be easily identified in the scattering map, which remains so for all wavelengths.

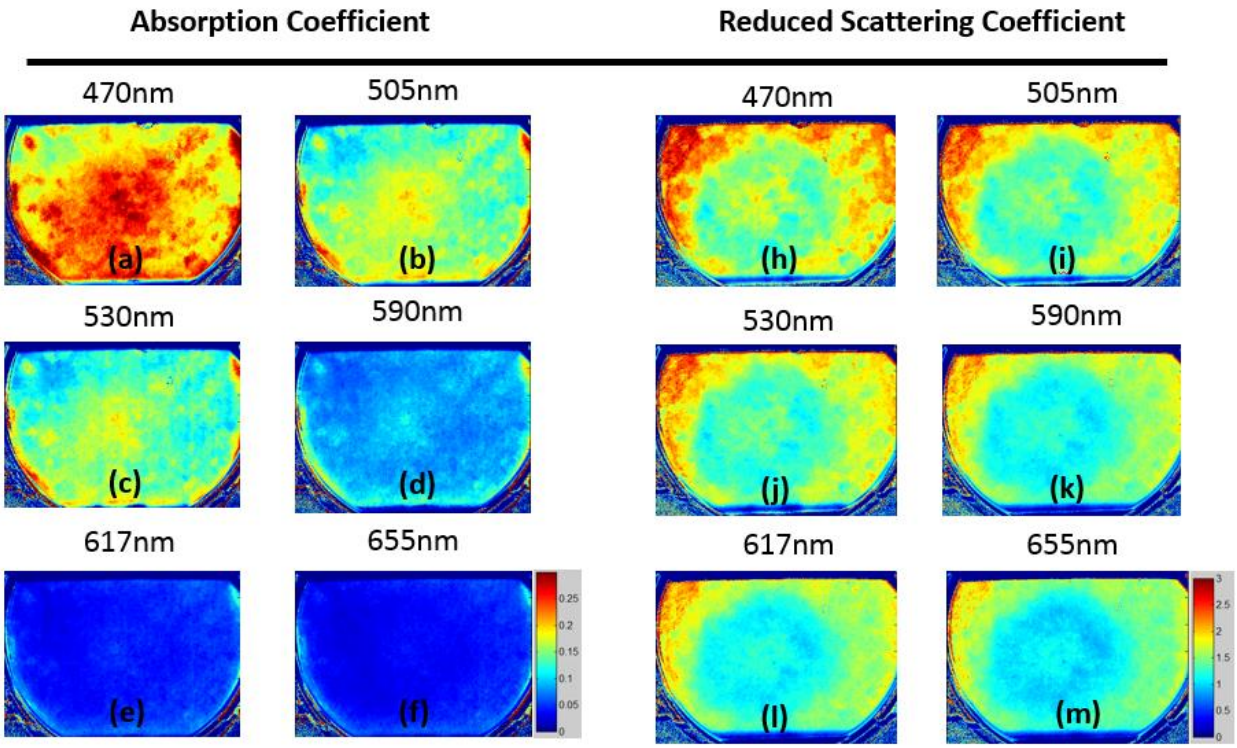

Figure 5.5 Absorption and reduced scattering coefficient maps for basal cell carcinoma (BCC) at six wavelengths

Based on absorption map, we further extracted total hemoglobin (Hb) and melanin concentration map for GA lesion, Fig. 5.6. Total Hb maps suggest that blood concentration is about 3 times higher in the lesion region than surrounding normal skin, which could be due to necrotizing inflammation that surrounds blood vessels. Unlike absorption map, the shape of the elevated Hb concentration matches well with the actual lesion shape. The melanin map suggested that elevated melanin concentration corresponded well with the pigmentation feature on the skin. The lesion can't be identified easily in melanin map.

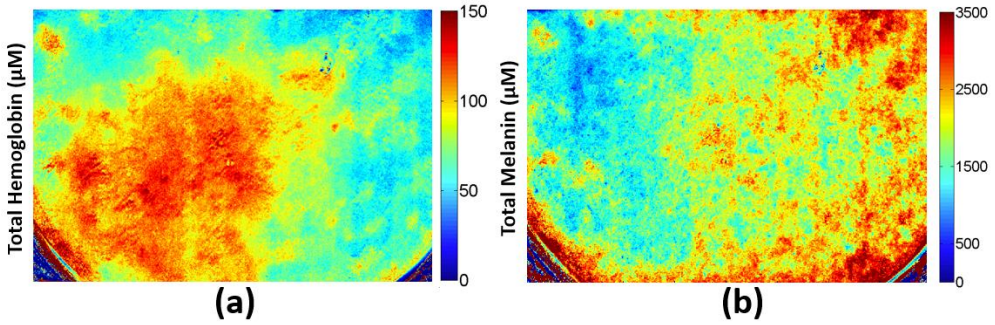

Figure 5.6 Total hemoglobin (Hb) and total melanin (Mel) concentration map of granuloma annulare lesion. The lesion shows elevated Hb concentration compared to surrounding normal tissue. Total Mel map agrees well with pigmented features on the skin

5.3.3 Absorption Reduced Fluorescence Imaging

The visual inspection on SK reveals that the lesion has distinct structural features compared with its surrounding normal skin tissue, Fig. 5.8(a). Furthermore, the lesion shows higher absorption than normal tissues. The raw fluorescence image shows the fluorescence from both normal skin and SK lesion, Fig. 5.8(b). Overall the fluorescence intensity are comparable between those two, although more structural features are visible on SK lesion. The raw fluorescence image may be mistakenly understood as lesion has similar fluorophore concentration compared with normal skin tissue. After we extracted the AC component from raw fluorescence images at $f = 0.6mm^{-1}$, and we noticed that the contrast between the lesion and the background was greatly enhanced, Fig. 5.8(c). The fluorescence from the lesion was so high that makes the fluorescence from normal tissue almost negligible. This could be understood as SK lesion is high fluorescent however it is also highly absorbing, which significantly reduces the fluorescence intensity from the lesion in

conventional fluorescence image. Furthermore, in demodulated image, SK lesion showed more structural features and better resolution.

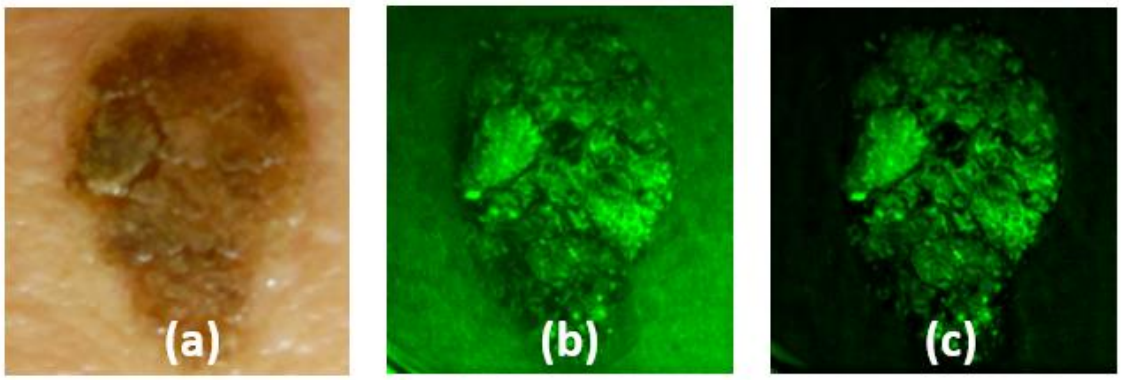

Figure 5.7(a) Color picture of seborrheic keratosis (SK) lesion (b) raw fluorescence image of SK (c) demodulated fluorescence image at f=0.6mm^{-1}

5.4 DISCUSSION AND CONCLUSION

In this paper, we described a SFDI imaging based clinical skin imaging system which performs both reflectance imaging and fluorescence imaging. The processed data provide comprehensive characterization on skin properties such as quantitative skin biochemical composition, absorption reduced fluorescence as well as color reflectance image that highlights the structural changes.

The excitation light source used in fluorescence imaging was at 395nm. Using a shorter wavelength such as 365nm will yield a stronger fluorescence, however, the optics in DMD evaluation module is not optimized for UV illumination. At 365nm, most of the excitation light were absorbed by optical components in the light engine most likely due to coating and the material itself. Even at 395nm, it took about 1.7 seconds to image one frame. The

fluorescence was collected over a wide emission band of 525nm-575nm. The collected fluorescence has a mixed contribution from multiple endogenous tissue fluorophore including collagen, NADH and keratin. The fluorescence imaging described in this paper was intended to quantify overall tissue fluorescence intensity instead of spectroscopic measurements.

Reflectance image at high spatial frequency provides a unique way to study skin diseases. By comparing the AC image with reduced scattering coefficient map, we can notice that these two images looks very similar. This may suggest that the AC image can used as a first order approximation of reduced scattering coefficient map; AC image can be used to examine structural changes when quantitative evaluation is not necessary. By extracting AC image, the structural changes not normally observed in DC images are highlighted. Especially, at longer wavelength (λ>600nm), the intrinsic absorption from hemoglobin and melanin is minimized, thus the contrast in AC image can be considered mainly from scattering/structural property changes. The color-rendered reflectance image provides intuitive visualization of the skin lesions as human eyes are more sensitive to color image than to grey scale image. Instead of providing color rendered still images, this technique can be easily implemented to achieve video rate visualization on skin lesions using the strategy previously described. In this case, a white light source and a color camera will be needed.

CHAPTER 6 : CONCLUSION

6.1 SUMMARY

In Chapter 2, I introduced a hybrid look-up table generation method to optical property quantification. Monte-Carlo simulation based approach and experimental approach are two main methods to generate LUT. Monte-Carlo simulation is cost efficient and flexible to simulation tissue response. It is able to provide 'generic' results under ideal condition which is imaging system independent. On the other hand, experimental approach can take system specific properties into account, such as light delivery and collection geometry and imaging environment, which improves quantification accuracy. However, experimental approach typically requires making a large set of tissue simulation phantom, typically more than 100 phantoms for good optical property coverage, which is costly; and more importantly phantom fabrication process inevitably introduces errors. The hybrid LUT generation methods integrates both MC simulation and experimental phantom measurement to improve the accuracy and reduce the cost. The LUT based on MC simulation serves as a starting pointing. By introducing phantom based calibration and scaling, 'generic' LUT is transformed to imaging system specific LUT. The results showed that the relative error for both absorption and reduced scattering coefficient extraction over a lager optical property range can be controlled well under 5%.

In Chapter 3, I described two SFDI technique based methods, ACFi and ARSFi to correct tissue attenuation in fluorescence imaging. In fluorescence imaging, imaged fluorescence intensity is affected by local fluorescence concentration as well as local attenuation

especially absorption. With attenuation, fluorescence intensity can't be directly related to fluorophore concentration, which complicates situations such tumor margin detection and treatment dosage optimization. To reduce the attenuation, two SFDI based strategies are exploited: model based correction using optical properties and experimental correction using high spatial frequency.

In the model based correction technique or ACF imaging, we utilized an attenuation correction model based on photon migration theory, which accounts for attenuation at both excitation and emission wavelengths. This technique was initially developed for spectra correction from a point measurement. We used SFDI imaging to quantify optical properties of the sample at both excitation and emission wavelength, which is the key to translate this technique to image based correction. The performance is robust. The fluorescence intensity drop was reduced to about 10% at highest absorption compared with over 80% drop before correction. Although accurate, it requires at least 7 individual images to derive all necessary quantities for correction. These images can't be acquired simultaneously, which makes imaging acquisition lengthy. Thus this method is more suited for static sample imaging instead of real-time imaging.

To achieve real-time attenuation, we utilized depth controlled imaging capability of SFDI imaging in ARSFi. As the spatial frequency increases, the effective imaging depth decreases by removing diffuse photons from deeper tissue. At a reduced imaging depth, the absorption from both excitation and emission is also reduced, which means fluorescence intensity is less affected by absorption. The absorption reduction is achieved by simply demodulating raw fluorescence images, which is not computationally intensive.

To make it real-time, we took the advantage of cyclic patterns, which means starting from the third frame, for each newly acquired raw fluorescence image, an ARSF image will be generated. Together with both software and hardware optimization, we achieved a frame rate of 19 frames/second. Although artifacts can be observed under relatively fast motion in the video, the video generally is smooth and stable.

In Chapter 4, I further exploited depth controlled imaging of SFDI to improve fiber orientation mapping accuracy in multi-layered samples by only imaging the superficial layer. Tissue microstructures, such as collagen fibers, play an important role in tissue function. As the tissue is under external loading, collagen fibers are stretched and rotate to bear to load. Thus quantifying collagen fiber orientation helps to understand structure-function relationship. Collagen fibers in many tissue types, such as connective tissue, display highly organized structures, which allows for using polarization techniques to study fiber properties. To understand the behavior of collagen fiber under polarized light illumination, we modeled collagen fiber as an infinite long circular cylinder. We studied the properties of polarization dependent back scattering from collagen fibers and noticed back scattering efficiency is higher when illumination polarization is parallel to local fiber orientation, and lower when they are perpendicular. By using this property, local fiber orientation can be easily mapped. However, using this technique in conventional reflectance imaging resulted in a depth averaged quantity, which is might be problematic in multi-layered samples. To improve the quantification accuracy, we chose to only imaging the superficial layer by introducing SFDI imaging. We demonstrated on an aortic heart valve leaflet that at a spatial frequency of $f=1mm^{-1}$, only fibrosa layer was imaged.

The fiber orientation map of fibrosa layer showed several differences compared with depth averaged results. Thus by integrating polarized light imaging and SFDI imaging, fiber orientation can be better quantified by physically limiting the imaging depth in superficial layer.

In Chapter 5, I developed a handheld SFDI imaging system for clinical skin characterization. Imaging techniques described in previous chapters were implemented in this handheld device including: optical property extraction, biochromophore concentration mapping, depth controlled imaging and absorption reduced fluorescence imaging. In current clinic practice, a dermatologist typically examines skin lesion using both naked eyes and using dermatoscope. By quantitatively evaluating skin lesion properties, more information can be provided towards more accurate clinical diagnosis. To facilitate clinical imaging, we separated light source from the imaging head and those two are connected by a flexible liquid light guide. The imaging head is very compact and can access most part of the body. The imaging time takes ~45 seconds depending on tissue type and the motion artifacts are well controlled by providing physical contact between imaging head and the skin. With the system, a total of 48 lesions from 31 patients, both benign and malignant, were images. We demonstrated the skin property characterization capability on three representative lesions: granuloma annulare (GA), basal cell carcinoma (BCC) and seborrheic keratosis (SK). We quantified optical properties, total hemoglobin and melanin concentration on GA. Furthermore, we generated color SFD image for GA and BCC. Compared to conventional color reflectance image, color SFD image reduced tissue absorption and highlighted tissue scattering property. Thus, skin lesion can be studies from

a new perspective. Finally, we demonstrated that ARSFi on SK enhanced fluorescence contrast between the lesion and surround normal skin.

6.2 FUTURE WORK

6.2.1 Optimization towards Compact SFDI Imaging Module

The core component of SFDI imaging technology is DMD module, which generates structured patterns. For each projected pattern, a reflectance image is recorded. The DMD allows for flexibility of generating structured patterns at any desired spatial frequency. However, for certain applications, the spatial frequency is fixed for optimal results. Under such circumstance, utilizing DMD solution may introduce adverse effects, and alternative solution may better fit those applications

The DMD module accounts for significance cost in SFDI system. For the system that we developed, we used most economic DMD solution, DLP LightCrafter, which costs $600. However, low cost comes with limitations. The resolution of this 0.3'' chipset is only 608*684. With this chipset, large projection area and high spatial frequency can't be achieved at same time. The pattern refresh rate at 8-bit grayscale can be up 120Hz. However, in SFDI application, synchronization between projection and image acquisition can significantly reduce the achievable refresh rate. This is because, 8-bit grayscale image is actually comprised of a number of 2-bit images. By changing duty cycle of each 2-bit image, the time integrated image appears an 8-bit grayscale image. When exposure time is close to inverse of pattern refresh rate, camera is able to resolve individual 2-bit grayscale

images, which creates artifacts. Both limitation can be mitigated with a larger and faster DMD chipset, however, the cost can easily over $10,000.

To further reduce the cost while improving the performance, one option is to replace DMD chipset with a spinning transparency filter. Three phase-shifted patterns are printed to a transparent substrate, thus, under the illumination, the pattern will be projected to the sample surface. As the transparency filter spins, the phase-shifted patterns will be projected one by one. By mounting the transparency filter to high speed motor, high speed imaging acquisition can be achieved using proper trigger mechanism. Although spatial frequency can't be changed after the pattern is printed, the projected spatial frequency still can be manipulated by changing the zoom ratio of the projection lens. This solution has the potential for highly compact design for pattern projection.

6.2.2 Imaging Acquisition Optimization for pSFDI Imaging

Comparing pSFDI with SALS, it is apparent that the imaging speed has been greatly improved. pSFDI imaging takes about 90 seconds to image a leaflet which typically takes hours for SALS imaging. However, for certain applications, 90 seconds imaging time may still be too slow. For example, to study tissue deformation under the controlled external loading, measurements will be taken at multiple loading condition. To reduce overall imaging time, the speed of pSFDI system needs to be further improved. The speed bottleneck of current system is from rotational stage. We adopted discrete motion, which means the polarizer rotates to a desired orientation and the orientation does not change until the imaging acquisition finishes. Although rotational stage is able to spin at a speed of 25

degree/second, the acceleration and deceleration for each discrete motion slows down overall performance. One approach to improve this is to adopt continuous motion with a high speed camera. Because the rotation is continuous, the exposure must integrates over an angular range $\Delta\theta$. Thus, total time t required to image over 180 degree can be express as

$$t > \frac{180}{FPS \cdot \Delta\theta} \tag{25}$$

where FPS (frame per second) quantifies how fast a camera can acquire images. To reduce the error, this integration angular range $\Delta\theta$ can be set to 1 degree. If the desired imaging time to be 10 second, FPS only needs to be 18 frames/second, and rotational speed is 18 degree/second. Also note that shorter imaging time requires both higher FPS of camera and faster rotary speed; or larger integration angular range, which adversely affects measurement accuracy. So while reducing imaging time is desired, it requires careful balance between improvement and potential costs.

References

1. K. J. Zuzak, M. D. Schaeberle, E. N. Lewis and I. W. Levin, "Visible reflectance hyperspectral imaging: characterization of a noninvasive, in vivo system for determining tissue perfusion," *Anal Chem* 74(9), 2021-2028 (2002)

2. T. Vo-Dinh, "A hyperspectral imaging system for in vivo optical diagnostics," *Engineering in Medicine and Biology Magazine, IEEE* 23(5), 40-49 (2004)

3. V. Ntziachristos, C. Bremer and R. Weissleder, "Fluorescence imaging with near-infrared light: new technological advances that enable in vivo molecular imaging," *European radiology* 13(1), 195-208 (2003)

4. J. V. Frangioni, "In vivo near-infrared fluorescence imaging," *Curr Opin Chem Biol* 7(5), 626-634 (2003)

5. S. L. Jacques, J. C. Ramella-Roman and K. Lee, "Imaging skin pathology with polarized light," *J Biomed Opt* 7(329 (2002)

6. W. Stummer, U. Pichlmeier, T. Meinel, O. D. Wiestler, F. Zanella, H.-J. Reulen and A.-G. S. Group, "Fluorescence-guided surgery with 5-aminolevulinic acid for resection of malignant glioma: a randomised controlled multicentre phase III trial," *The lancet oncology* 7(5), 392-401 (2006)

7. B. E. Schaafsma, J. S. D. Mieog, M. Hutteman, J. R. Van der Vorst, P. J. Kuppen, C. W. Löwik, J. V. Frangioni, C. J. Van de Velde and A. L. Vahrmeijer, "The clinical use of indocyanine green as a near-infrared fluorescent contrast agent for image-guided oncologic surgery," *Journal of surgical oncology* 104(3), 323-332 (2011)

8. B. S. Sorg, B. J. Moeller, O. Donovan, Y. Cao and M. W. Dewhirst, "Hyperspectral imaging of hemoglobin saturation in tumor microvasculature and tumor hypoxia development," *J Biomed Opt* 10(044004 (2005)

9. L. L. Randeberg, E. L. P. Larsen and L. O. Svaasand, "Characterization of vascular structures and skin bruises using hyperspectral imaging, image analysis and diffusion theory," *J Biophotonics* 3(1-2), 53-65 (2010)

10. T. G. Bromage, H. M. Goldman, S. C. McFarlin, J. Warshaw, A. Boyde and C. M. Riggs, "Circularly polarized light standards for investigations of collagen fiber orientation in bone," *The Anatomical Record Part B: The New Anatomist* 274(1), 157-168 (2003)

11. T. T. Tower, M. R. Neidert and R. T. Tranquillo, "Fiber alignment imaging during mechanical testing of soft tissues," *Ann Biomed Eng* 30(10), 1221-1233 (2002)

12. L. Larsen, L. D. Griffin, D. GRäßel, O. W. Witte and H. Axer, "Polarized light imaging of white matter architecture," *Microscopy research and technique* 70(10), 851-863 (2007)

13. G. Themelis, J. S. Yoo, K. S. Soh, R. Schulz and V. Ntziachristos, "Real-time intraoperative fluorescence imaging system using light-absorption correction," *J Biomed Opt* 14(064012 (2009)

14. M. E. Martin, M. B. Wabuyele, K. Chen, P. Kasili, M. Panjehpour, M. Phan, B. Overholt, G. Cunningham, D. Wilson and R. C. DeNovo, "Development of an advanced hyperspectral imaging (HSI) system with applications for cancer detection," *Ann Biomed Eng* 34(6), 1061-1068 (2006)

15. S. Alali and A. Vitkin, "Polarized light imaging in biomedicine: emerging Mueller matrix methodologies for bulk tissue assessment," *J Biomed Opt* 20(6), 061104-061104 (2015)

16. D. J. Cuccia, F. Bevilacqua, A. J. Durkin and B. J. Tromberg, "Modulated imaging: quantitative analysis and tomography of turbid media in the spatial-frequency domain," *Opt. Lett* 30(11), 1354-1356 (2005)

17. L. V. Wang and H.-i. Wu, *Biomedical optics: principles and imaging*, Wiley. com (2012).

18. J. Folkman, "Angiogenesis in cancer, vascular, rheumatoid and other disease," *Nature medicine* 1(1), 27-30 (1995)

19. V. Backman, M. Wallace, L. Perelman, J. Arendt, R. Gurjar, M. Müller, Q. Zhang, G. Zonios, E. Kline and T. McGillican, "Detection of preinvasive cancer cells," *Nature* 406(6791), 35-36 (2000)

20. D. J. Cuccia, F. Bevilacqua, A. J. Durkin, F. R. Ayers and B. J. Tromberg, "Quantitation and mapping of tissue optical properties using modulated imaging," *J Biomed Opt* 14(2), 024012-024012-024013 (2009)

21. T. A. Erickson, A. Mazhar, D. Cuccia, A. J. Durkin and J. W. Tunnell, "Lookup-table method for imaging optical properties with structured illumination beyond the diffusion theory regime," *J Biomed Opt* 15(036013 (2010)

22. A. Ponticorvo, E. Taydas, A. Mazhar, C. L. Ellstrom, J. Rimler, T. Scholz, J. Tong, G. R. Evans, D. J. Cuccia and A. J. Durkin, "Evaluating visual perception for assessing reconstructed flap health," *J Surg Res* (2015)

23. A. Mazhar, S. Saggese, A. C. Pollins, N. L. Cardwell, L. Nanney and D. J. Cuccia, "Noncontact imaging of burn depth and extent in a porcine model using spatial frequency domain imaging," *J Biomed Opt* 19(8), 086019-086019 (2014)

24. D. J. Rohrbach, N. C. Zeitouni, D. Muffoletto, R. Saager, B. J. Tromberg and U. Sunar, "Characterization of nonmelanoma skin cancer for light therapy using spatial frequency domain imaging," *Biomedical Optics Express* 6(5), 1761-1766 (2015)

25. I. Georgakoudi, B. C. Jacobson, M. G. Müller, E. E. Sheets, K. Badizadegan, D. L. Carr-Locke, C. P. Crum, C. W. Boone, R. R. Dasari and J. Van Dam, "NAD (P) H and collagen as in vivo quantitative fluorescent biomarkers of epithelial precancerous changes," *Cancer Res* 62(3), 682-687 (2002)

26. S. Keereweer, J. D. F. Kerrebijn, P. B. A. A. van Driel, B. Xie, E. L. Kaijzel, T. J. A. Snoeks, I. Que, M. Hutteman, J. R. van der Vorst and J. S. D. Mieog, "Optical Image-guided Surgery—Where Do We Stand?," *Molecular Imaging and Biology* 13(2), 199-207 (2011)

27. G. M. van Dam, G. Themelis, L. M. A. Crane, N. J. Harlaar, R. G. Pleijhuis, W. Kelder, A. Sarantopoulos, J. S. de Jong, H. J. G. Arts and A. G. J. van der Zee, "Intraoperative tumor-specific fluorescence imaging in ovarian cancer by folate receptor-[alpha] targeting: first in-human results," *Nature medicine* (2011)

28. G. Themelis, A. Sarantopoulos, N. J. Harlaar, G. M. Dam and V. Ntziachristos, "Real-time intra-operative fluorescence imaging with targeted fluorophores," Optical Society of America (2010).

29. M. G. Müller, I. Georgakoudi, Q. Zhang, J. Wu and M. S. Feld, "Intrinsic fluorescence spectroscopy in turbid media: disentangling effects of scattering and absorption," *Appl Optics* 40(25), 4633-4646 (2001)

30. Q. Zhang, M. G. Müller, J. Wu and M. S. Feld, "Turbidity-free fluorescence spectroscopy of biological tissue," *Opt Lett* 25(19), 1451-1453 (2000)

31. J. Wu, M. S. Feld and R. P. Rava, "Analytical model for extracting intrinsic fluorescence in turbid media," *Appl Optics* 32(19), 3585-3595 (1993)

32. N. Biswal, S. Gupta, N. Ghosh and A. Pradhan, "Recovery of turbidity free fluorescence from measured fluorescence: an experimental approach," *Opt Express* 11(24), 3320-3331 (2003)

33. K. L. Billiar and M. S. Sacks, "Biaxial mechanical properties of the native and glutaraldehyde-treated aortic valve cusp: part II—a structural constitutive model," *Journal of biomechanical engineering* 122(4), 327-335 (2000)

34. M. S. Sacks, D. B. Smith and E. D. Hiester, "A small angle light scattering device for planar connective tissue microstructural analysis," *Ann Biomed Eng* 25(4), 678-689 (1997)

35. D. J. Cuccia, F. Bevilacqua, A. J. Durkin, F. R. Ayers and B. J. Tromberg, "Quantitation and mapping of tissue optical properties using modulated imaging," *J Biomed Opt* 14(2), (2009)

36. W. F. Cheong, S. A. Prahl and A. J. Welch, "A Review of the Optical-Properties of Biological Tissues," *Ieee J Quantum Elect* 26(12), 2166-2185 (1990)

37. L. Wang, S. L. Jacques and L. Zheng, "MCML—Monte Carlo modeling of light transport in multi-layered tissues," *Comput Meth Prog Bio* 47(2), 131-146 (1995)

38. E. Alerstam, W. C. Y. Lo, T. D. Han, J. Rose, S. Andersson-Engels and L. Lilge, "Next-generation acceleration and code optimization for light transport in turbid media using GPUs," *Biomedical optics express* 1(2), 658 (2010)

39. I. S. Saidi, S. L. Jacques and F. K. Tittel, "Mie and Rayleigh modeling of visible-light scattering in neonatal skin," *Appl Optics* 34(31), 7410-7418 (1995)

40. C. F. Poh, L. Zhang, D. W. Anderson, J. S. Durham, P. M. Williams, R. W. Priddy, K. W. Berean, S. Ng, O. L. Tseng and C. MacAulay, "Fluorescence visualization detection of field alterations in tumor margins of oral cancer patients," *Clin Cancer Res* 12(22), 6716-6722 (2006)

41. N. Thekkek and R. Richards-Kortum, "Optical imaging for cervical cancer detection: solutions for a continuing global problem," *Nat Rev Cancer* 8(9), 725-731 (2008)

42. J. de Leeuw, N. van der Beek, W. D. Neugebauer, P. Bjerring and H. Neumann, "Fluorescence detection and diagnosis of non-melanoma skin cancer at an early stage," *Laser Surg Med* 41(2), 96-103 (2009)

43. N. Rajaram, J. S. Reichenberg, M. R. Migden, T. H. Nguyen and J. W. Tunnell, "Pilot clinical study for quantitative spectral diagnosis of non-melanoma skin cancer," *Laser Surg Med* 42(10), 716-727 (2010)

44. M. Mogensen and G. B. E. Jemec, "Diagnosis of nonmelanoma skin cancer/keratinocyte carcinoma: A review of diagnostic accuracy of nonmelanoma skin cancer diagnostic tests and technologies," *Dermatol Surg* 33(10), 1158-1174 (2007)

45. P. Lane, S. Lam, M. Follen and C. MacAulay, "Oral fluorescence imaging using 405-nm excitation, aiding the discrimination of cancers and precancers by identifying changes in collagen and elastic breakdown and neovascularization in the underlying stroma," *Gender medicine* 9(1), S78-S82. e78 (2012)

46. I. Georgakoudi, B. C. Jacobson, M. G. Müller, E. E. Sheets, K. Badizadegan, D. L. Carr-Locke, C. P. Crum, C. W. Boone, R. R. Dasari and J. Van Dam, "NAD (P) H and collagen as in vivo quantitative fluorescent biomarkers of epithelial precancerous changes," *Cancer Res* 62(3), 682 (2002)

47. D. Roblyer, R. Richards-Kortum, K. Sokolov, A. K. El-Naggar, M. D. Williams, C. Kurachi and A. M. Gillenwater, "Multispectral optical imaging device for in vivo detection of oral neoplasia," *J Biomed Opt* 13(2), 024019-024019-024011 (2008)

48. P. Lee, R. M. van den Berg, S. Lam, A. F. Gazdar, K. Grunberg, A. McWilliams, J. LeRiche, P. E. Postmus and T. G. Sutedja, "Color fluorescence ratio for detection of bronchial dysplasia and carcinoma in situ," *Clin Cancer Res* 15(14), 4700-4705 (2009)

49. S. Keereweer, H. Sterenborg, J. Kerrebijn, P. Van Driel, R. De Jong and C. Löwik, "Image-guided surgery in head and neck cancer: Current practice and future directions of optical imaging," *Head & Neck* 34(1), 120-126 (2012)

50. R. S. Kramer and R. D. Pearlstein, "Cerebral cortical microfluorometry at isosbestic wavelengths for correction of vascular artifact," *Science* 205(4407), 693-696 (1979)

51. R. Richards-Kortum, R. P. Rava, M. Fitzmaurice, L. L. Tong, N. B. Ratliff, J. R. Kramer and M. Feld, "A one-layer model of laser-induced fluorescence for diagnosis of disease in human tissue: applications to atherosclerosis," *Biomedical Engineering, IEEE Transactions on* 36(12), 1222-1232 (1989)

52. A. Durkin, S. Jaikumar, N. Ramanujam and R. Richards-Kortum, "Relation between fluorescence spectra of dilute and turbid samples," *Appl Optics* 33(3), 414-423 (1994)

53. G. Zonios, L. T. Perelman, V. Backman, R. Manoharan, M. Fitzmaurice, J. Van Dam and M. S. Feld, "Diffuse Reflectance Spectroscopy of Human Adenomatous Colon Polyps In Vivo," *Appl Optics* 38(31), 6628-6637 (1999)

54. S. T. Flock, S. L. Jacques, B. C. Wilson, W. M. Star and M. J. C. van Gemert, "Optical properties of Intralipid: a phantom medium for light propagation studies," *Laser Surg Med* 12(5), 510-519 (1992)

55. B. J. Tromberg, A. Mazhar, D. J. Cuccia, S. Gioux, A. J. Durkin and J. V. Frangioni, "Structured illumination enhances resolution and contrast in thick tissue fluorescence imaging," *J Biomed Opt* 15(1), (2010)

56. J. V. Frangioni, S. Gioux, A. Mazhar, D. J. Cuccia, A. J. Durkin and B. J. Tromberg, "Three-dimensional surface profile intensity correction for spatially modulated imaging," *J Biomed Opt* 14(3), (2009)

57. J. Vervandier and S. Gioux, "Single snapshot imaging of optical properties," *Biomedical optics express* 4(12), 2938-2944 (2013)

58. K. P. Nadeau, A. J. Durkin and B. J. Tromberg, "Advanced demodulation technique for the extraction of tissue optical properties and structural orientation contrast in the spatial frequency domain," *J Biomed Opt* 56013(1 (2014)

59. D. Arifler, I. Pavlova, A. Gillenwater and R. Richards-Kortum, "Light scattering from collagen fiber networks: micro-optical properties of normal and neoplastic stroma," *Biophys J* 92(9), 3260-3274 (2007)

60. E. M. Joyce, J. Liao, F. J. Schoen, J. E. Mayer Jr and M. S. Sacks, "Functional collagen fiber architecture of the pulmonary heart valve cusp," *The Annals of thoracic surgery* 87(4), 1240-1249 (2009)

61. M. S. Sacks, "Biaxial mechanical evaluation of planar biological materials," *Journal of elasticity and the physical science of solids* 61(1-3), 199-246 (2000)

62. M. S. Sacks, "Incorporation of experimentally-derived fiber orientation into a structural constitutive model for planar collagenous tissues," *Journal of biomechanical engineering* 125(2), 280 (2003)

63. R. Drezek, A. Dunn and R. Richards-Kortum, "Light scattering from cells: finite-difference time-domain simulations and goniometric measurements," *Appl Optics* 38(16), 3651-3661 (1999)

64. T. T. Tower and R. T. Tranquillo, "Alignment maps of tissues: I. Microscopic elliptical polarimetry," *Biophys J* 81(5), 2954-2963 (2001)

65. R. Liao, N. Zeng, X. Jiang, D. Li, T. Yun, Y. He and H. Ma, "Rotating linear polarization imaging technique for anisotropic tissues (Journal Paper)," *J Biomed Opt* 15(03), 036014 (2010)

66. S. Jiao and L. V. Wang, "Two-dimensional depth-resolved Mueller matrix of biological tissue measured with double-beam polarization-sensitive optical coherence tomography," *Opt Lett* 27(2), 101-103 (2002)

67. H. Axer and D. G. v Keyserlingk, "Mapping of fiber orientation in human internal capsule by means of polarized light and confocal scanning laser microscopy," *Journal of neuroscience methods* 94(2), 165-175 (2000)

68. T. Yasui, Y. Tohno and T. Araki, "Determination of collagen fiber orientation in human tissue by use of polarization measurement of molecular second-harmonic-generation light," *Appl Optics* 43(14), 2861-2867 (2004)

69. S. D. Konecky, T. Rice, A. J. Durkin and B. J. Tromberg, "Imaging scattering orientation with spatial frequency domain imaging," *J Biomed Opt* 16(12), 126001-1260018 (2011)

70. S. Alali, M. Ahmad, A. Kim, N. Vurgun, M. F. G. Wood and I. A. Vitkin, "Quantitative correlation between light depolarization and transport albedo of various porcine tissues," *J Biomed Opt* 17(045004 (2012)

71. Z. Nan, J. Xiaoyu, G. Qiang, H. Yonghong and M. Hui, "Linear polarization difference imaging and its potential applications," *Appl Optics* 48(35), 6734-6739 (2009)

72. C. F. Bohren and D. R. Huffman, *Absorption and scattering of light by small particles*, John Wiley & Sons (2008).

73. H. C. Hulst and H. Van De Hulst, *Light scattering by small particles*, Courier Dover Publications (1957).

74. M. Sacks and C. Chuong, "Characterization of collagen fiber architecture in the canine diaphragmatic central tendon," *Journal of biomechanical engineering* 114(2), 183-190 (1992)

75. M. S. Sacks, D. B. Smith and E. D. Hiester, "The aortic valve microstructure: effects of transvalvular pressure," *Journal of biomedical materials research* 41(1), 131-141 (1998)

76. C.-H. Lee, P. J. Oomen, J. P. Rabbah, A. Yoganathan, R. C. Gorman, J. H. Gorman III, R. Amini and M. S. Sacks, "A high-fidelity and micro-anatomically accurate 3d finite element model for simulations of functional mitral valve," in *Functional Imaging and Modeling of the Heart*, pp. 416-424, Springer (2013).

77. L. Bozec, G. van der Heijden and M. Horton, "Collagen fibrils: nanoscale ropes," *Biophys J* 92(1), 70-75 (2007)

78. S. P. Morgan, Q. Zhu, I. M. Stockford and J. A. Crowe, "Rotating orthogonal polarization imaging," *Opt Lett* 33(13), 1503-1505 (2008)

79. S. F. Bish, N. Rajaram, B. Nichols and J. W. Tunnell, "Development of a noncontact diffuse optical spectroscopy probe for measuring tissue optical properties," *J Biomed Opt* 16(12), 120505-1205053 (2011)

80. L. Lim, B. Nichols, M. R. Migden, N. Rajaram, J. S. Reichenberg, M. K. Markey, M. I. Ross and J. W. Tunnell, "Clinical study of noninvasive in vivo melanoma and nonmelanoma skin cancers using multimodal spectral diagnosis," *J Biomed Opt* 19(11), 117003-117003 (2014)

81. M. Sharma, E. Marple, J. Reichenberg and J. W. Tunnell, "Design and characterization of a novel multimodal fiber-optic probe and spectroscopy system for skin cancer applications," *Rev Sci Instrum* 85(8), 083101 (2014)

82. S. F. Bish, M. Sharma, Y. Wang, N. J. Triesault, J. S. Reichenberg, J. X. Zhang and J. W. Tunnell, "Handheld Diffuse Reflectance Spectral Imaging (DRSi) for in-vivo characterization of skin," *Biomedical optics express* 5(2), 573-586 (2014)

83. R. Saager, D. Cuccia, S. Saggese, K. Kelly and A. Durkin, "A Light Emitting Diode (LED) Based Spatial Frequency Domain Imaging System for Optimization of Photodynamic Therapy of Nonmelanoma Skin Cancer: Quantitative Reflectance Imaging," *Laser Surg Med* 45(4), 207-215 (2013)

84. A. Mazhar, S. A. Sharif, J. D. Cuccia, J. S. Nelson, K. M. Kelly and A. J. Durkin, "Spatial frequency domain imaging of port wine stain biochemical composition in response to laser therapy: A pilot study," *Laser Surg Med* 44(8), 611-621 (2012)

85. B. Yang and J. W. Tunnell, "Real-time absorption reduced surface fluorescence imaging," *J Biomed Opt* 19(9), 090505-090505 (2014)

86. K. Wolff and R. Johnson, "Fitzpatrick's Color Atlas And Synopsis Of Clinical Dermatology: (Fitzpatrick's Color Atlas & Synopsis O," (2009)